



**HAL**  
open science

## Validation of an integrated satellite-data-driven response to an effusive crisis: the April–May 2018 eruption of Piton de la Fournaise

Andrew J.L. J.L. Harris, Magdalena Oryaëlle Chevrel, Diego Coppola, Michael Ramsey, Alexis Hrysiewicz, Simon Thivet, Nicolas Villeneuve, Massimiliano Favalli, Aline Peltier, Philippe Kowalski, et al.

### ► To cite this version:

Andrew J.L. J.L. Harris, Magdalena Oryaëlle Chevrel, Diego Coppola, Michael Ramsey, Alexis Hrysiewicz, et al.. Validation of an integrated satellite-data-driven response to an effusive crisis: the April–May 2018 eruption of Piton de la Fournaise. *Annals of Geophysics*, 2019, 61 (Vol 61 (2018)), 10.4401/ag-7972 . hal-02150627

**HAL Id: hal-02150627**

**<https://sde.hal.science/hal-02150627>**

Submitted on 7 Jun 2019

**HAL** is a multi-disciplinary open access archive for the deposit and dissemination of scientific research documents, whether they are published or not. The documents may come from teaching and research institutions in France or abroad, or from public or private research centers.

L'archive ouverte pluridisciplinaire **HAL**, est destinée au dépôt et à la diffusion de documents scientifiques de niveau recherche, publiés ou non, émanant des établissements d'enseignement et de recherche français ou étrangers, des laboratoires publics ou privés.



ACCEPTED ON ANNALS OF GEOPHYSICS, 61, 2018; Doi:  
10.4401/ag-7972

## Validation of an integrated satellite-data-driven response to an effusive crisis: the April–May 2018 eruption of Piton de la Fournaise

Andrew J.L. Harris<sup>1</sup>, Magdalena Oryaelle Chevrel<sup>1</sup>, Diego Coppola<sup>2</sup>, Michael S. Ramsey<sup>3</sup>, Alexis Hrysiewicz<sup>1</sup>, Simon Thivet<sup>1</sup>, Nicolas Villeneuve<sup>4</sup>, Massimiliano Favalli<sup>5</sup>, Aline Peltier<sup>6</sup>, Philippe Kowalski<sup>6</sup>, Andrea Di Muro<sup>6</sup>, Jean-Luc Froger<sup>1</sup>, Lucia Gurioli<sup>1</sup>

<sup>1</sup> Université Clermont Auvergne, CNRS, OPGC, Laboratoire Magmas et Volcans, 63000 Clermont-Ferrand, France.

<sup>2</sup> Dipartimento di Scienze della Terra, Università degli Studi di Torino, Via Valperga Caluso 35, 10125 Torino, Italy.

<sup>3</sup> Department of Geology and Planetary Science, University of Pittsburgh, Pittsburgh, PA, USA

<sup>4</sup> Laboratoire GeoSciences Reunion, Université de La Reunion, Institut de Physique du Globe de Paris, Sorbonne Paris Cité, CNRS, F-97744 Saint Denis, France.

<sup>5</sup> Istituto Nazionale di Geofisica e Vulcanologia (INGV), Via della Faggiola, 32, 56126 Pisa, Italy.

<sup>6</sup> Observatoire Volcanologique du Piton de la Fournaise (OVPF), Institut de Physique du Globe de Paris, Sorbonne Paris Cité, Univ. Paris Diderot, CNRS, F-97418 La Plaine des Cafres, La Reunion, France.

1 Validation of an integrated satellite-data-driven response to an effusive crisis:  
2 the April–May 2018 eruption of Piton de la Fournaise

3 Andrew J.L. Harris<sup>1</sup>, Magdalena Oryaëlle Chevrel<sup>1</sup>, Diego Coppola<sup>2</sup>, Michael S. Ramsey<sup>3</sup>, Alexis  
4 Hrysiewicz<sup>1</sup>, Simon Thivet<sup>1</sup>, Nicolas Villeneuve<sup>4</sup>, Massimiliano Favalli<sup>5</sup>, Aline Peltier<sup>6</sup>, Philippe  
5 Kowalski<sup>6</sup>, Andrea Di Muro<sup>6</sup>, Jean-Luc Froger<sup>1</sup>, Lucia Gurioli<sup>1</sup>

6 1. Université Clermont Auvergne, CNRS, OPGC, Laboratoire Magmas et Volcans, 63000 Clermont-  
7 Ferrand, France.

8 2. Dipartimento di Scienze della Terra, Università degli Studi di Torino, Via Valperga Caluso 35, 10125  
9 Torino, Italy.

10 3. Department of Geology and Planetary Science, University of Pittsburgh, Pittsburgh, PA, USA

11 4. Laboratoire GéoSciences Réunion, Université de La Réunion, Institut de Physique du Globe de  
12 Paris, Sorbonne Paris Cité, CNRS, F-97744 Saint Denis, France.

13 5. Istituto Nazionale di Geofisica e Vulcanologia (INGV), Via della Faggiola, 32, 56126 Pisa, Italy.

14 6. Observatoire Volcanologique du Piton de la Fournaise (OVPF), Institut de Physique du Globe de  
15 Paris, Sorbonne Paris Cité, Univ. Paris Diderot, CNRS, F-97418 La Plaine des Cafres, La Réunion,  
16 France.

17 **Abstract.** Satellite-based surveillance of volcanic hot spots and plumes can be coupled with  
18 modeling to allow ensemble-based approaches to crisis response. We complete benchmark tests on  
19 an effusive crisis response protocol aimed at delivering product for use in tracking lava flows. The  
20 response involves integration of four models: MIROVA for discharge rate (TADR), the ASTER urgent  
21 response protocol for delivery of high-spatial resolution satellite data, DOWNFLOW for flow path  
22 projections, and PyFLOWGO for flow run-out. We test the protocol using the data feed available  
23 during Piton de la Fournaise’s April–May 2018 eruption, with product being delivered to the  
24 Observatoire du Piton de la Fournaise via Google Drive. The response was initialized by an alert at  
25 19:50Z on 27 April 2018. Initially DOWNFLOW-FLOWGO were run using TADRs typical of Piton de la  
26 Fournaise, and revealed that flow at  $>120 \text{ m}^3/\text{s}$  could reach the island belt road. The first TADR (10–  
27  $20 \text{ m}^3/\text{s}$ ) was available at 09:55Z on 28 April, and gave flow run-outs of 1180–2510 m. The latency  
28 between satellite overpass and TADR provision was 105 minutes, with the model result being posted  
29 15 minutes later. An InSAR image pair was completed six hours after the eruption began, and gave a  
30 flow length of 1.8 km; validating the run-out projection. Thereafter, run-outs were updated with  
31 each new TADR, and checked against flow lengths reported from InSAR and ASTER mapping. In all,  
32 35 TADRs and 15 InSAR image pairs were processed during the 35-day-long eruption, and 11 ASTER  
33 images were delivered.

34 **Introduction**

35 Throughout the 1990’s and 2000’s methods were developed to extract lava flow discharge rates from  
36 1 km spatial resolution satellite data collected by satellite sensors operating in the thermal infrared  
37 (e.g., Harris et al., 1997; 2007; Harris & Bologna 2009; Coppola et al., 2010). At the same time, high  
38 spatial resolution (30 m) satellite data were shown to be of value for mapping lava flow fields (e.g.,

39 Flynn et al., 1994; Wright et al., 2000; Lombardo et al., 2009), with InSAR data allowing estimation of  
40 lava flow areas, thicknesses and, hence, volumes (e.g., Zebker et al., 1996; Rowland et al., 1999; Lu et  
41 al., 2003). In parallel, a series of lava flow models were developed to allow flow inundation areas to  
42 be simulated (e.g., Young & Wadge, 1990; Crisci et al., 2003; Vicari et al., 2007). Increasingly, the  
43 capabilities have been merged to allow an ensemble-based approach whereby satellite data from  
44 multiple wavelengths and spatial resolutions are combined to allow maximum constraint and cross-  
45 validation (e.g., Patrick et al., 2003; Rowland et al., 2003; Wright et al., 2005) and source term input  
46 into real-time lava flow emplacement models (e.g., Wright et al., 2008; Vicari et al., 2011; Ganci et  
47 al., 2016). Since 2015, just such a response model has been developed at Piton de la Fournaise  
48 (Harris et al. 2017), where we here review and validate an updated version of the protocol so as to  
49 review an ensemble approach to responding to an effusive crisis.

50 The response protocol is based on *in situ* observations and data acquisitions carried out routinely by  
51 the Observatoire du Piton de la Fournaise (OVPF) team and the integration of four models: MIROVA  
52 (Coppola et al. 2016), the ASTER (Advanced Spaceborne Thermal Emission Radiometer) urgent  
53 response protocol (Ramsey, 2016), DOWNFLOW (Favalli et al., 2005) and FLOWGO (Harris and  
54 Rowland, 2001). MIROVA is a near-real time hot spot detection system that uses MODIS data, and  
55 has been calibrated for TADR calculation at Piton de la Fournaise by Coppola et al. (2010), the ASTER  
56 urgent response protocol is a means of automatically prioritizing and targeting ASTER data  
57 acquisition during a volcanic eruption. Instead, while DOWNFLOW is a stochastic model that  
58 assesses potential flow paths based on iterative runs over a DEM with random noise added, FLOWGO  
59 can calculate the cooling-limit of flow down each path (Rowland et al., 2005; Wright et al., 2008). To  
60 estimate the maximum distance a flow can extend at a given effusion rate, FLOWGO tracks the  
61 thermal and rheological evolution of a control volume of lava as it moves down a channel, tracking  
62 the volume until the volume cools and crystallizes to such an extent that forward motion becomes  
63 rheologically impossible (Harris and Rowland 2015). FLOWGO has been initialized for and tested for  
64 lava channels at Piton de la Fournaise by Harris et al. (2016) and Rhéty et al. (2017), and—to allow  
65 improved model initialization, iteration and application—has been rewritten and rebuilt in Python as  
66 PyFLOWGO (Chevrel et al., 2018). It is this version of FLOWGO that we use here.

67 As described in Harris et al. (2017), the response protocol is initialized with the alert of an imminent  
68 eruption and provision of the vent location provided by the OVPF as part of their mandated  
69 monitoring and response procedures. Subsequently, it involves calling each model in sequence and  
70 passing results between each actor, and then final product to OVPF, in as timely fashion as possible.  
71 The protocol also calls in ground truth (for vent locations, effusion rates, channel dimensions, flow  
72 lengths) provided by the OVPF as well as textural and chemical data (for eruption temperatures,  
73 vesicularity, crystallinity, rheological models) produced at LMV, to improve model uncertainty and  
74 syn-response validation. We show here how the response protocol works, and define the main  
75 uncertainties, using a real-time exercise held immediately after the April–May 2018 eruption of Piton  
76 de la Fournaise. The aim of the exercise was to refine model initialization and execution for Piton de  
77 la Fournaise, reduce uncertainty, and to fully define the call-down and communication protocol. It  
78 involved first following the data feed and executing responses, in the order that they were received,  
79 followed by a validation phase in which remote sensing and model based estimates for discharge  
80 rate and flow length were compared against ground truth. In doing so, we show how an integrated  
81 multi-sensor remote sensing approach can be used to follow, document and quantify an effusive  
82 event in near-real time.

### 83 **The April–May 2018 eruption of Piton de la Fournaise and available data**

84 The April–May 2018 eruption of Piton de la Fournaise began late on 27 April (19h50 UTC) from five  
85 north-south orientated en-echelon fissures that opened between the elevations of 2165 m and 2285  
86 m on the southwest flank of the terminal cone (Figure 1a). Initially flow was channel-fed 'a'a which  
87 moved down the SW flank of the Dolomieu. In a short time activity reached a peak and became  
88 focused at a main vent roughly central to the fissure line at an elevation of 2200 m. Another much  
89 less active vent a few meters to the north continued to project tephra and emit flames. Around the  
90 two vents, scoria cones and tephra fields were constructed. Upon reaching the base of the Enclos  
91 Fouqué wall (between the 29 and 30 April), lava flows turned southeast to follow the base of the wall  
92 reaching a distance of 2.6 km before discharge rates declined and active flow fronts retreated to  
93 positions closer to the vent (Figure 1b). Between 4 and 7 May, flow activity was concentrated in the  
94 proximal section of the flow field with several tubes and, with two main zones of breakout being  
95 active 200 and 500 m down the tube system (Figure 1c). Breakouts from the tube system fed low-  
96 discharge rate flows which extended no more than 100–200 m. From 7 May new lava flows broke out  
97 from an ephemeral vent at the base of the Enclos Fouqué Southern wall producing local vegetation  
98 fires. Over the following days, the tube continued to extend and feed lava flows from its terminus, so  
99 that by 10 May the tube exit was around 3.2 km from the vent. This continued to feed low-discharge  
100 rate flows that extended over 1.1 km (or 4.5 km from the main vent) along the base of the Enclos  
101 Fouqué wall. Activity continued in this way until 1 June 2018 when activity died out around 14h30  
102 (local time). During the 34.6-day-long eruption, six aerial photograph, two aerial IR image and  
103 several field observation campaigns, including GPS measurements, lava and tephra sampling, gas  
104 analysis and UAV over flights were completed by the OVPF. In addition, 35 cloud-free MODIS images,  
105 11 ASTER images and 15 InSAR image pairs all of which were available for near-real time analysis and  
106 reporting.

### 107 **Methodology**

108 While implementation of MIROVA and the ASTER urgent response protocol (URP) allow near-real  
109 time collection and processing of satellite thermal data for derivation of time-averaged discharge  
110 rate and mapping of a thermal anomaly, DOWNFLOW and FLOWGO (DOWNFLOWGO) allow the flow  
111 paths and potential run out distance to be projected. These models are called in sequence, where  
112 the call-down procedure is given in Figure 2. As part of this system, output and product are shared  
113 using a standardized reporting form (as given in Appendix A) which is shared between an email  
114 distribution list involving all actors in the response chain, and to OVPF for integration into  
115 surveillance and reporting duties. With each update, the group is issued an update email, flagging  
116 the field that has been updated and giving the time and date of the update as well as the name of  
117 the person responsible for the update. The reporting form has four fields for: (i) current MIROVA-  
118 derived TADR and time series; (ii) current vent location and DOWNFLOWGO projections; (iii) current  
119 ASTER thermal distribution map, with flow field evolution time series and report; (iv) InSAR-based  
120 flow length report and coherence images (Appendix A). Another field may be added to the reporting  
121 form including relevant OVPF data collection, e.g., flow length from Structure from Motion (SfM),  
122 SO<sub>2</sub> flux, sampling locations etc. This is left at the observatory's discretion to add depending on work  
123 loads and time commitment.

124 MIROVA and ASTER were called using the observatory bulletin announcing implementation of alert  
125 level 1, that is an eruption is believed (on the basis of seismic and ground deformation data) to be  
126 “imminent” (in the next minutes/hours). This causes ASTER to be targeted, and MIROVA to set up a  
127 “watch” for the first sign of a hot spot. Upon eruption onset, DOWNFLOWGO is run as soon as vent  
128 location(s) (GPS coordinates) is (are) known. The first vent location is usually provided by OVPF  
129 personnel or gendarmerie using hand-held GPS from a helicopter which is flown by the police  
130 (gendarmerie) service. Precision may vary depending on flight time available, the height of the  
131 fountains and the number of aircraft in the air space above the eruption site. Initially, to give an  
132 immediate idea of likely flow paths and inundation areas, 10000 flow lines are run to the edge of the  
133 DEM (i.e., the coast) over the most recent 5-m DEM with random noise of between  $\pm 0.8$  m and  $\pm 2.5$   
134 m being added between each run. The slope from the line of steepest descent (LoSD) at  $\pm 0.001$  m is  
135 then extracted (and smoothed every 10 m) and used for preliminary FLOWGO runs at various  
136 effusion rates (10, 20, 30, 40, 50, to 100 m<sup>3</sup>/s). To do this, FLOWGO is initialized prior to the call  
137 down using typical Piton de la Fournaise thermo-rheological conditions and textural properties as  
138 given in Table 1. At the beginning of the eruption, a typical channel width of 4 m is taken (Table 1),  
139 and the model iterates on depth until the combination with calculated velocity gives the required  
140 effusion rate. Subsequently, upon derivation of a first TADR from MIROVA, the cooling-limited  
141 extent of flow down each flow line is then updated. Runs driven by the MIROVA-derived TADR are  
142 then plotted over a Piton de la Fournaise base map to give an idea of how the flow front may extend,  
143 or retreat, if TADRs increase (or decrease) over the current level. In addition, if vent location or  
144 channel width information are updated or made available, these are also modified and all models re-  
145 run.

146 Upon receipt of the first ASTER imagery a thermal anomaly map is produced, and flow locations and  
147 lengths assessed on the basis of the spatial distribution of spectral radiance in 90 m ASTER band 12  
148 (thermal infrared, 8.925–9.275  $\mu\text{m}$ ). In addition, vent location is checked where the intense thermal  
149 anomaly at the vent is apparent in ASTER band 3 (near-infrared, 0.807  $\mu\text{m}$ ) image. The 15 m-pixel  
150 size, and one pixel accuracy of the geolocation, allows the location of the vent hot spot to  $\pm 15$  m.  
151 This is often better than that provided by hand-held GPS, which when run in a fast moving helicopter  
152 records a point that will lag behind the craft point by several hundred meters. If this is the case, the  
153 vent location is updated and new DOWNFLOWGO runs are produced. If tubes begin to extend from  
154 the vent, this—following Wright et al. (2000)—becomes apparent in the high spatial resolution  
155 satellite images from the distribution of spectral radiance. In such as case, the source for  
156 DOWNFLOWGO will be moved to the tube exit.

157 In addition, InSAR interferograms and SfM data are processed for flow thickness and length maps  
158 that both add to the information flow and allow validation of model-based flow-length projections.  
159 Although remaining largely underutilized in an operational response sense, the value of such data in  
160 producing lava flow thickness maps as long been known (e.g., Zebker et al., 1996; Rowland et al.,  
161 1999; MacKay et al., 1998; Stevens, 2002; Lu et al., 2003), as has the potential for merging with  
162 ancillary data, such as thermal-IR-derived TADRs and model-based lava flow run-outs (Rowland et al.,  
163 2003). The InSAR method consists of computing an interferogram by subtracting the phase between  
164 two SAR images acquired for the same area at different times (for details of the method see  
165 Appendix B). These statistics which are input into a fourth field in the reporting form (Appendix A)  
166 and are also used to update the DEM used for flow path runs.

## 167 Validation

168 On 4 May 2018 an over flight was made in an ultra-light aircraft at a flight height of around 310 m  
169 above the ground surface. A thermal camera was used to collect 52 images of the lava flow field and  
170 vent system between 12:15 and 12:30 local time. The thermal camera was a FLIR Systems T650  
171 which provides a  $640 \times 480$  pixel image in the 8–14  $\mu\text{m}$  waveband, with 0.65 mrad pixels. This, over  
172 a line-of-sight distance of 460 m (and viewing angle of  $48^\circ$ ) gives a pixel size of 0.3 m. Images were  
173 used to obtain vent (eruption) temperatures and down channel surface temperature profiles to use  
174 in FLOWGO, as well as channel and flow dimensions plus radiative ( $Q_{\text{rad}}$ ), convective ( $Q_{\text{conv}}$ ) and total  
175 ( $Q_{\text{tot}} = Q_{\text{rad}} + Q_{\text{conv}}$ ) heat fluxes to check against model output. In addition, the MODIS and ASTER  
176 images collected at 10:30 (local time) on the same day (i.e., two hours previously) were fitted to the  
177 thermal camera image mosaic to allow the heat fluxes and TADRs to be compared. TADR was  
178 extracted from the thermal camera images using  $\text{TADR} = Q_{\text{tot}} / \rho (c_p \Delta T + f\Lambda)$ , in which  $\rho$  is the lava  
179 density,  $c_p$  is specific heat capacity,  $\Delta T$  is the cooling range,  $f$  is the fraction of crystals grown down  
180 flow and  $\Lambda$  is latent heat of crystallization. Values characteristic of recent lavas at Piton de la  
181 Fournaise were used for  $\rho$ ,  $c_p$ , and  $f$ , these being  $2079 \text{ kg/m}^3$ ,  $1225 \text{ J/kg K}$  and 0.1, respectively, with a  
182 cooling range of 75–250  $^\circ\text{C}$  (Harris et al. 2007). At the end of the eruption, following sample analysis,  
183 the chemical, temperature, crystallinity and vesicularity sections of the initialization file for flow  
184 modeling are checked, and if necessary, updated (Table 1).

## 185 Results

186 The trigger for the protocol of Figure 2 was the Bulletin released by OVPF on 27 April 2018 at 20h30  
187 local time (16h30 UTC). The bulletin declared that a seismic crisis had begun at 20h15 local time  
188 (16h15 UTC) accompanied by rapid ground deformation indicative of “magma leaving the storage  
189 system and propagating towards the surface” (Peltier 2018). Consequently, an eruption was  
190 declared probable in the following minutes or hours, and the alert level was set to “Alert 1” (Peltier  
191 2018). As a result, the MIROVA “watch” began at 20h30 (16h30 UTC) on 27 April, with an ASTER URP  
192 being triggered at 04h25 (00h25 UTC) on 29 April (Appendix C). In addition, on receipt of the  
193 Bulletin, DOWNFLOWGO was loaded with the most recent DEM of Piton de la Fournaise, this being  
194 the 5-m DEM generated from LiDAR data in 2010 modified by adding the largest flow fields in the  
195 area that are the October 2010 and the August 2015 using the InSAR-based thickness maps.

196 The eruption began at 23h50 local time (19h50 UTC) on 27 April. Initially DOWNFLOWGO was run  
197 from a vent location set on the basis of fissure location relative to pre-existing topographic features  
198 as apparent in images acquired by OVPF’s web-cam monitoring network. For this case, the camera  
199 used was that of “Piton Bert” (BERC, <http://www.ipgp.fr/fr/ovpf/reseau-de-cameras>) which targets  
200 this sector of the volcano. Comparison of a daytime image as a background layer and an image  
201 acquired during the eruption revealed the fissure to approximately extend between two newly  
202 formed cinder cones at an elevation of 2200 m on the SW flank of the terminal cone. These cones  
203 were located at 365375 m E; 7649065 m S and 365500 m E; 7848455 m S, and DOWNFLOW was  
204 launched from a point between the two cones at 365377 m E; 7648853 m S. This showed that the  
205 flows would likely move SW down the flank of the terminal cone, and then turn SE to following the  
206 caldera wall to the coast (Figure 3). The effusion rate contour map for this case was subsequently  
207 produced and posted on the reporting form (Figure 3). This revealed that flows fed at sustained  
208 rates in excess of  $120 \text{ m}^3/\text{s}$  were capable of reaching the island belt road, to reach the coast.

209 However, because a 4 km wide basin existed after a distance of 4 km from the vent, flows became  
210 held up at this point, with even flows at  $80 \text{ m}^3/\text{s}$  coming to a halt 4 km from the vent; and to push the  
211 model across the basin needed more than  $120 \text{ m}^3/\text{s}$ . Thus, in reality, our prediction was that either  
212 time would be needed to fill this basin, where lava needed time spread and pile up, and/or for a tube  
213 to develop across the basin—a little like the case of lava flow advance towards Etna Zafferana in  
214 1992 (Barberi et al. 1993).

215 The first cloud-free MODIS overpass occurred at 09h55 (UTC, 13h55 local time) on 28 April, i.e.,  
216 around 14 hours after the eruption began. This yielded a TADR of  $10\text{--}20 \text{ m}^3/\text{s}$  (Table 2). These  
217 values were immediately input into the reporting sheet, thereby being handed onwards for input  
218 into the PyFLOWGO initialization file. The first lava flow projection map was thus also completed and  
219 posted; revealing flows were capable of extending up to 1180–2510 m under initial conditions  
220 (Figure 4a). The latency between satellite overpass and TADR provision was 105 minutes, with the  
221 model result being posted 15 minutes later. The first S1B InSAR image pair was completed around six  
222 hours after the eruption began and was also entered into the reporting sheet (Figure 5a). These  
223 revealed that the flow was already 1.8 km long and covered an area of  $0.5\pm 0.1 \times 10^6 \text{ m}^2$  (Table 3);  
224 giving an initial extension rate of around 5 m/min and coverage rate of  $1400 \text{ m}^2/\text{min}$ . On the same day,  
225 at 09h00 (local time), the first SfM survey was completed and by 16h00 (local time) approximate  
226 location of the fissures and flow outline from aerial images were published by the OVPF.

227 At 03h33 (UTC, 07h33 local time) on 30 April, after a new aerial visit of the eruption, the center of  
228 the main fissure was precisely given at 365365 m E; 7648810 m S. By this time, however, MODIS-  
229 derived TADR had declined to  $3.7\text{--}6.9 \text{ m}^3/\text{s}$  (Table 2). Updating PyFLOWGO revealed reduced run-  
230 outs of 0.7–1.0 km. The first cloud-free ASTER image was acquired on 2 May. This revealed an 11  
231 pixel-long anomaly of saturated pixels orientated NE-SW on the south flank of the Dolomieu (Figure  
232 6)—equivalent to a 990 m long zone of active lava (Table 4). The active vent was apparent as a single  
233 pixel hot spot in the 15-m near-infrared data and the vent location was updated to 365280 m E;  
234 7648835 m S (Appendix D), with the TADR for this day being  $3.6\text{--}4.6 \text{ m}^3/\text{s}$  (Table 2). These details  
235 were updated in the reporting form, and the vent location for DOWNFLOWGO adjusted slightly  
236 (although this had no effect on the flow paths or LoSD). The following day (3 May), the second  
237 coherence map was produced. This revealed that the lava flow field had, at some point, reached the  
238 base of the caldera wall, turning SE to follow the base of the wall (Figure 6) having attained a length  
239 of 2.5 km (Table 3). The shorter length of the active flows implied by the size of the thermal anomaly  
240 in ASTER on 2 May, as well as the 17 pixel (1530 m) long zone of cooler pixels beyond the front of the  
241 main hot spot indicated that flow front locations had begun to retreat back up flow by this time.

242 The thermal camera imagery obtained from the over-flight of 4 May confirmed that activity had  
243 diminished, and comprised tube-fed breakouts of channel-fed 'a'a (Figure 1c). Two main breakouts  
244 were located where the southern breakout was fed by a 2 m-wide channel which fed a 110 m pad of  
245 'a'a. Total heat flux from the breakout was  $435\pm 50 \text{ MW}$ , which converted to a TADR of  $0.61\text{--}1.65$   
246  $\text{m}^3/\text{s}$ . ASTER imagery revealed that, by 9 May, the tube had extended 2430 m (Figure 6) to feed lava  
247 flows of around 1.4 km in length. At the same time, MIROVA revealed continued decline in TADR  
248 (Figure 7) to between 1 and  $2 \text{ m}^3/\text{s}$ . As a result, the vent location for DOWNFLOW was moved to the  
249 tube exit, which ASTER gave as being at 364685 m E; 7647090 m S, and FLOWGO run at 1.6 and  $3.8$   
250  $\text{m}^3/\text{s}$  (Table 2) with an updated channel width and eruption temperature (Table 1). This gave flow  
251 lengths of 1–2 km beyond the end of the tube system (Figure 4b).



252 Thereafter, TADRs remained at low levels (Figure 7) and the flow field continued to build parallel with  
253 the base of the caldera wall (Figure 5). TADRs of  $0.8 \text{ m}^3/\text{s}$  characteristic of the final week of the  
254 eruption (Table 2) gave flow lengths that extended just 1 km from the end of the tube (Figure 4b).  
255 The flow field (both predicted and measured) attained a final length of 4.1 km and area of  $1.3 \pm 0.1 \times$   
256  $10^6 \text{ m}^2$  (Table 3), and a volume of  $5.5 \pm 1.6 \times 10^6 \text{ m}^3$  (Table 2). In all, 35 TADR sets were processed by  
257 MIROVA (Table 2), 15 image pairs were processed for coherence analysis (Table 3), 11 ASTER images  
258 were obtained using the ASTER URP (Table 4) and DOWNFLOWGO was launched three times as TADR  
259 and vent location changed. Additionally, six aerial photograph data sets, two aerial IR image surveys  
260 and multiple field observations, including lava and tephra sampling, gas analyses, UAV over flights  
261 were completed by the OVPF. The final reporting sheet, filled out with all derived values from this  
262 data set, is given in Appendix D.

## 263 Discussion

264 The aerial survey mapping of the flow field of 30 April allowed checking of the dimensions of the lava  
265 flow field derived from InSAR data; the center line length being 1.8 km (the same as that given by  
266 InSAR) and the area having excellent coincidence with the zone of incoherence obtained from the  
267 InSAR data. Likewise, dimensions of InSAR zones of incoherence, ASTER thermal anomalies and  
268 FLOWGO lengths are in excellent agreement (Figure 8). For example, the thermal anomaly in ASTER  
269 on 2 May revealed that flows had extended to a maximum distance of 2520 m in the preceding  
270 days. This compares with the 2.5 km long zone of incoherence recorded by the InSAR pair processed  
271 the following day (3 May) and the 2510 m flow length generated by FLOWGO using the maximum  
272 TADRs obtained from MIROVA the first few days of the eruption. Closing the circle with validation of  
273 the FLOWGO run outs with good fits with dimensions of incoherence and thermal anomalies in InSAR  
274 and ASTER data gives us confidence in the source terms (including MIROVA-derived TADR) entered  
275 into the model. We next assess the uncertainty in those MIROVA-derived TADR, as well as the  
276 FLOWGO run-outs and errors due to DEM problems.

### 277 Validation of MIROVA-derived TADR

278 The image collected on 4 May by MODIS-MIROVA indicates a total radiant power ( $Q_{\text{rad}}$ ) of  $497 \pm 149$   
279 MW, corresponding to a total TADR of  $2.6 \pm 0.6 \text{ m}^3/\text{s}$ . Total radiant power is around 42 % of that  
280 measured for the south breakout on 4 May using the thermal camera (i.e.,  $209 \pm 20$  MW). The TADR  
281 ( $1.13 \pm 0.52 \text{ m}^3/\text{s}$ ) obtained from the thermal image is also 43 % that of the MODIS-MIROVA,  
282 indicating confidence in the latter value and the conversion routine used. In this regard, MODIS-  
283 MIROVA uses the conversion  $Q_{\text{rad}}/\text{TADR} = c_{\text{Rad}}$  (Coppola et al. 2010). For Piton de la Fournaise,  
284 Coppola et al. (2010) used thermal camera data for the May–June 2003 eruption to obtain  $c_{\text{Rad}}$  of  
285  $2.5 \pm 1 \times 10^8 \text{ J m}^{-3}$ . The value of  $c_{\text{Rad}}$  obtained here is  $2.3 \pm 1 \times 10^8 \text{ J m}^{-3}$  indicating that the conversion  
286 factor is stable, still holds and provides a TADR in good agreement with ground truth.

### 287 FLOWGO Uncertainty

288 To test uncertainty, we take our initial run of 28 April which was initialized with a TADR of  $20 \text{ m}^3/\text{s}$   
289 and vary the source terms of Table 1 within reasonable limits. Using the generic source terms of  
290 Table 1, the model solved for a channel depth of 4 m give a distance of 2510 m (Figure 4a).

291 Our first uncertainty is in eruption temperature. Thermal camera imagery of the vent on 4 May  
292 yielded maximum temperatures of up to  $1210\pm 40$  °C, a value which is suspiciously high. On 10 May,  
293 similarly suspicious temperatures of 1700 °C were recorded over a small skylight at the base of the  
294 main scoria cone. These temperatures are higher than the liquidus for Piton de la Fournaise and  
295 therefore cannot correspond to lava temperatures. However, nighttime observations revealed  
296 flames over the vent, so this appears to be a flame temperature, where the presence of the flame  
297 likely explains the intense thermal anomaly in the ASTER NIR band. Flame-free maxima were  
298  $1142\pm 35$  °C, consistent with temperatures obtained from the glass chemistry. If we update the  
299 eruption from 1114 °C temperature to 1142 °C (and readjust the channel dimension to balance for  
300 similar TADR) this increases the run out by just 30 m, revealing that a 3 % uncertainty in eruption  
301 temperature results in a 1 % uncertainty in run out.

302 Our second uncertainty is in bubble content and crystallinity and associated rheology models. Based  
303 on our analysis of lava samples from the 2015 channel, bubble content could be as high as 50 vol.%  
304 and phenocryst content as low as 1 vol.%. Because we use a simple two phase (fluid+crystals)  
305 mixture model bubble content effects the velocity equation through its effect on density, while the  
306 lower starting crystal content reduces the viscosity of the mixture. While increasing the vesicularity  
307 to 50 vol.% decreases run-out by 120 m (11 %), decreasing the phenocryst content to 1 vol.%  
308 increases run-out by 470 m (28 %).

309 The third uncertainty is on surface temperature which controls heat loss and hence cooling rate. We  
310 have used the typical effective radiation temperature approximated from the data of Flynn and  
311 Mougini-Mark (1994) for a lava channel on Kilauea to initialize the model (Table 1). The thermal  
312 imagery of the south break out channel indicates that this may be a little low, where temperatures  
313 down the center line are 520–890 °C, with a mean and standard deviation of 740 °C and 80 °C. If we  
314 use this mean temperature for the effective radiation temperature, we have a flow length that  
315 decreases by 230 m (23 %).

316 Our final uncertainty is on channel width. If, for example, we reduce to a width of 2 m, depth and  
317 velocity have to increase to 1.1 m and 4.8 m/s to balance the TADR. This yields a runout of 2550 m  
318 or 46 % longer, so that an uncertainty on channel depth of 50 % yields uncertainty on runout of the  
319 same order. However, to extent uncertainties may cancel. If for example, we increase the  
320 vesicularity to 50 vol.% but decrease the phenocryst content to 1 vol.% we change the runout by just  
321 50 m (for the same TADR). Likewise, if we decrease channel width to 2 m, but increase surface  
322 temperature to 740 °C we change the runout by 50 m. Thus, our error appears to be around 4-5 %,  
323 so that the error on a predicted runout of 3000 m, is just less than a few hundred meters.

#### 324 DEM uncertainty

325 Until now, for the near real time response at the effusive crises at Piton de la Fournaise, DOWNFLOW  
326 was run on the SRTM DEM from 2005. When we first ran the DOWNFLOW simulation (in May), the  
327 LoSD was not south to the base of the Enclos Fouqué wall, but projected due East. It was not possible  
328 to simulate the actual flow path because post-2005 topography could not be accounted for.  
329 However, now that we have updated our flow projection by using the 5-m 2010 DEM to which lava  
330 flow fields from October 2010 and August 2015 (which were both in the southern area of the Enclos  
331 Fouqué) were added, the predicted path is south, moving around the western edge of the 2015 flow  
332 field, and to reach the wall before flowing to the east along its base. This was exactly the trajectory of

333 the flow. Note that although the eruptive fissures were located near and onto the February 2015  
334 flow (on the distal part) we did not update the DEM with this lava flow as it did not interfere with the  
335 ongoing flow process. To model flows on a very active volcano, where topography is constantly  
336 changing, we thus need a DEM that is updated after each eruption, so as to reduce uncertainties on  
337 predicted flow inundation area.

338 To obtain the inundation area, DOWNFLOW needs to be calibrated to a specific scenario, and this is  
339 achieved by tuning N and Dh (Favalli et al. 2011). Previous simulations that were compared with real  
340 cases at Piton de la Fournaise showed that N=10000 and Dh of 2.5 m gives a good approximation of  
341 the proximal area around the Dolomieu, while a Dh of 0.8 m gives a better estimation of the lava  
342 flow distal, coastal zone. Subsequently, to obtain the LoSD, DOWNFLOW is first run with 1000  
343 iterations at Dh=1 mm which allows pits and holes to be filled. This filled DEM is then used to obtain  
344 a second LoSD with N=1 and Dh=0.001). Down the LoSD a slope value is extracted every 10 m for use  
345 in PyFLOWGO. PyFLOWGO includes traps for cases where slope values are negative or zero, where  
346 the slope is recalculated at each step from the average of the five previous and five following positive  
347 and non-zero values down the LoSD (Chevrel et al. 2018). This allows FLOWGO to overcome small  
348 terrain irregularities, and to project across holes and pits as well as flat zones. The value of 10 m has  
349 been chosen from several simulations and seems to be the best suited value. Although precise DEMs  
350 are always preferred, we find we have to smooth the LoSD in order to obtain results in agreement  
351 with reality.

352 In the present case, the changes in vent location between the first estimation and the coordinates  
353 obtained in the field or from the satellite images did not change significantly. The effect on the  
354 predicted flow path was therefore minor and limited to within 100 m of the vent area. However,  
355 knowing, and moving to, the break out location of 9 May, was essential to predict the final flow  
356 length (at the given new TADR). The protocol we are offering here, that is sharing ASTER, MODIS, and  
357 DOWNFLOWGO allow a back and forth to update the vent location and is therefore of major  
358 improvement for correct estimation of the lava flow path and runout distance. In addition this  
359 protocol is of service to OVPF to aid in monitoring needs for lava flow field evolution allowing both  
360 crisis management and appraisal of need to evacuate ground based monitoring stations falling in  
361 flow paths.

## 362 **Conclusion**

363 With the near-real time availability of data from so many satellite-based sensors, as well as the  
364 immediate availability of ground truth through upload to internet-based data hubs, the best way  
365 forward to tracking an effusive crisis is an ensemble-based approach. Such a system is open to  
366 expansion and ingestion of further data sets to improve coverage and further reduce lags between  
367 event and measurement. For example, VIIRS (Visible Infrared Imaging Radiometer Suite) can be  
368 considered as an extension to MODIS (Blackett 2015), and Sentinel-2 as an extension to ASTER  
369 (Cappello et al. 2018), with other sensors being incorporated as they come on-line. In this regard,  
370 technology is constantly evolving with new potential coming-on line every year where, for this case,  
371 we have begun to convolve data from sensors flown on UAVs, as well as from crowdsourcing.  
372 Another developing avenue is small, low cost satellite networks, such as the small satellite  
373 Technology Experiment Carrier-1 (TET-1) as developed by the German Aerospace Center and  
374 dedicated to monitoring high temperature events (Zhukov et al. 2006). Such systems offer high

375 spatial resolution (160 m) thermal infrared imagery at a relatively high temporal resolution (3 days)  
376 and have shown to be of value in tracking effusive crises yielding TADR time series to supplement  
377 those provided by MODIS (Zakšek et al. 2005).

378 As shown here, merging thermal data of different resolutions allows time series generation with the  
379 best possible temporal resolution and precision; cross-validation of TADR, error and uncertainty  
380 assessment; and input into lava flow emplacement models. The next step will be the use of InSAR  
381 data to allow DEMs to be updated between eruptions so as to ensure that flow paths are correct and  
382 use the most up-to-date topography available, with the DEM evolving as the topography changes.  
383 This is a key feature, especially during a long-term eruption with changing topography and vent  
384 position. In turn, the chain can be inverted where good agreement of model-predicted flow lengths  
385 with dimensions of thermal and incoherence anomalies in high spatial resolution and thermal data  
386 suggests that the source terms input into the model are valid. Another key feature explored here is  
387 immediate delivery of a flow run out map that considers all feasible TADRs. This means that delivery  
388 of the hazard map, which can be created in a few minutes, does not have to be attendant on the  
389 first, cloud-free satellite overpass for delivery of a TADR. Instead, the map gives the hazard manager  
390 an immediate idea of possible event scenario's which can be assessed and checked when the first  
391 TADR comes in, and updated as vent locations and topographies change.

392

393 **Acknowledgments.** This work comes out of a three day workshop and exercise held in Clermont  
394 Ferrand in June 2018 funded by ANR-LAVA. This work was funded by the Agence National de la  
395 Recherche (ANR: [www.agence-nationale-recherche.fr](http://www.agence-nationale-recherche.fr)) through project ANR-LAVA (ANR Program:  
396 DS0902 2016; Project: ANR-16 CE39-0009, PI: A. Harris, Link: [www.agence-nationale-recherche.fr/?Project=ANR-16-CE39-0009](http://www.agence-nationale-recherche.fr/?Project=ANR-16-CE39-0009); <https://sites.google.com/view/anrlava/>). We would like  
397 to thank the Sentinel-1 ESA team, especially P. Potin and Y.-L. Desnos for having made possible  
398 routine Sentinel-1 StripMap acquisition on La Réunion Island. This is ANR-LAVA contribution no. 5  
399 and IPGP contribution no. XXX.

401

## 402 **References**

403 Favalli M, Pareschi MT, Neri A, Isola I (2005) Forecasting lava flow paths by a stochastic approach.

404 *Geophys Res Lett*, 32(L03305). doi: 10.1029/2004GL021718

405 Flynn LP, Mougini-Mark PJ (1994) Temperature measurements of an active lava channel from

406 spectral measurements, Kilauea Volcano, Hawaii. *Bulletin of Volcanology*, 56, 297-301

407 Harris AJL, Rowland SK (2001) FLOWGO: a kinematic thermo-rheological model for lava flowing in a

408 channel. *Bull Volcanol*, 63, 20–44. doi:10.1007/s004450000120.

409 Harris AJL, Baloga SM (2009) Lava discharge rates from satellite-measured heat flux. *Geophys. Res.*

410 *Lett.*, 36, L19302. doi:10.1029/2009GL039717

411 Harris AJL, Rowland SK (2015) FLOWGO 2012: an updated framework for thermorheological

412 simulations of channel-contained lava. In: Carey, R., Cayol, V., Poland, M., Weis, D. (Eds.),

413 Hawaiian Volcanoes: from Source to Surface, Geophysical Monograph, vol. 208. American  
414 Geophysical Union, 457–481

415 Harris AJL, Blake S, Rothery DA, Stevens NF (1997) A chronology of the 1991 to 1993 Etna eruption  
416 using AVHRR data: Implications for real time thermal volcano monitoring, *J. Geophys. Res.*,  
417 102(B4), 7985–8003. doi:10.1029/96JB03388

418 Harris AJL, Dehn J, Calvari S (2007) Lava effusion rate definition and measurement: a review. *Bull*  
419 *Volcanol*, 70, 1–22

420 Harris A, Rhéty M, Gurioli L, Villeneuve N, Paris R. (2016) Simulating the thermorheological evolution  
421 of channel-contained lava: FLOWGO and its implementation in EXCEL. In: Harris AJL, De Groeve T,  
422 Garel F, Carn SA, editors. *Detecting, modelling and responding to effusive eruptions*, vol. 426.  
423 London: Geological Society, London Special Publication, 313–36. doi:10.1144/SP426.9.

424 Barberi F, Carapezz ML, Valenza M, Villari L (1993) The control of lava flow during the 1991–1992  
425 eruption of Mt. Etna. *Journal of Volcanology and Geothermal Research*, 56(1–2), 1-34.

426 Blackett M (2015) An initial comparison of the thermal anomaly detection products of MODIS and  
427 VIIRS in their observation of Indonesian volcanic activity. *Remote Sensing of Environment*, 171,  
428 75-82

429 Cappello A, Ganci G, Bilotta G, Herault A, Zago V, Del Negro C (2018) Satellite-driven modeling  
430 approach for monitoring lava flow hazards during the 2017 Etna eruption. *Annals of Geophysics*,  
431 61, Doi:10.4401/ag-7792

432 Chevrel MO, Labroquère J, Harris AJL, Rowland SK (2018) PyFLOWGO: An open-source platform for  
433 simulation of channelized lava thermo-rheological properties. *Computers & Geosciences*, 111,  
434 167–180

435 Coppola D, James MR, Staudacher T, Cigolini C (2010) A comparison of field- and satellite-derived  
436 thermal flux at Piton de la Fournaise: implications for the calculation of lava discharge rate. *Bull*  
437 *Volcanol.*, 72(3), 341–56. doi:10.1007/s00445-009-0320-8

438 Coppola D, Laiolo M, Cigolini C, Delle Donne D, Ripepe M (2016) Enhanced volcanic hot-spot  
439 detection using MODIS IR data: results from the MIROVA system. In: Harris AJL, De Groeve T,  
440 Garel F, Carn SA, editors. *Detecting, Modelling and responding to effusive eruptions*, vol. 426.  
441 London: Geological Society, London, Special Publications, 181–205.  
442 <http://doi.org/10.1144/SP426.5>.

443 Crisci G, Di Gregorio S, Rongo R, Scarpelli M, Spataro W, Calvari S (2003) Revisiting the 1669 Etnean  
444 eruptive crisis using a cellular automata model and implications for volcanic hazard in the Catania  
445 area. *Journal of Volcanology and Geothermal Research*, 123, 211-230.

446 Flynn LP, Mougini-Mark PJ, Horton KA (1994) Distribution of thermal areas on an active lava flow  
447 field: Landsat observations of Kilauea, Hawaii, July 1991. *Bull. Volcanol.*, 56, 284-296.

448 Ganci G, Bilotta G, Cappello A, Herault A, Del Negro C (2016) HOTSAT: a multiplatform system for the  
449 thermal monitoring of volcanic activity using satellite data. In Harris, A. J. L., De Groeve, T., Garel,

450 F. & Carn, S. A. (eds) 2016. Detecting, Modelling and Responding to Effusive Eruptions. Geological  
451 Society, London, Special Publications, 426, 207–221. First published online October 29, 2015,  
452 <http://doi.org/10.1144/SP426.21>

453 Lombardo V, Harris AJL, Calvari S, Buongiorno MF (2009) Spatial variations in lava flow field thermal  
454 structure and effusion rate derived from very high spatial resolution hyperspectral (MIVIS) data. *J.*  
455 *Geophys. Res.*, 114, B02208. doi:10/1029.2008JB005648

456 Lu Z, Fielding E, Patrick MR, Trautwein CM (2003) Estimating lava volume by precision combination of  
457 multiple baseline spaceborne and airborne interferometric synthetic aperture radar: The 1997  
458 eruption of Okmok volcano, Alaska. *IEEE Transactions on Geoscience and Remote Sensing* ,41(6),  
459 1428-1436.

460 MacKay ME, Rowland SK, Mouginiis-Mark PJ, Gareil H (1998) Thick lava flows of Karisimbi volcano,  
461 Rwanda: insights from SIR-C interferometric topography. *Bull. Volcanol.*, 60, 239-251.

462 Patrick MR, Dehn J, Papp KR, Lu Z, Dean K, Moxey L, Izbekov P, Guritz R (2003) The 1997 eruption of  
463 Okmok Volcano, Alaska: a synthesis of remotely sensed imagery. *J Volcanol Geotherm Res*, 127,  
464 87–105

465 Peltier A (2018) Bulletin du 27 avril 2018 – 20:30 heure locale Observatoire Volcanologique du Piton  
466 de la Fournaise. Bulletin of the Observatoire Volcanologique du Piton de la Fournaise, 27 April  
467 2018, OVPF\_20180427\_20h30- ISSN 2610-5101.

468 Ramsey M (2016) Enhanced volcanic hot-spot detection using MODIS IR data: results from the  
469 MIROVA system. In: Harris AJL, De Groot T, Garel F, Carn SA, editors. Detecting, Modelling and  
470 responding to effusive eruptions, vol. 426. London: Geological Society, London, Special  
471 Publications, 181–205. <http://doi.org/10.1144/SP426.5>.

472 Rhéty M, Harris A, Villeneuve N, Gurioli L, Médard E, Chevrel O, Bachélery P (2017) A comparison of  
473 cooling-limited and volume-limited flow systems: Examples from channels in the Piton de la  
474 Fournaise April 2007 lava-flow field, *Geochem. Geophys. Geosyst.*, 18,  
475 doi:10.1002/2017GC006839.

476 Rowland SK, MacKay ME, Garbeil H, Mouginiis-Mark PJ (1999) Topographic analyses of Kilauea  
477 volcano, Hawaii, from interferometric airborne radar. *Bull. Volcanol.*, 61, 1-14.

478 Rowland SK, Harris AJL, Wooster MJ, Amelung F, Garbeil H, Wilson L, Mouginiis-Mark PJ (2003)  
479 Volumetric characteristics of lava flows from interferometric radar and multispectral satellite  
480 data: the 1995 Fernandina and 1998 Cerro Azul eruptions in western Galápagos. *Bull. Volcanol.*,  
481 65, 311-330.

482 Rowland SK, Garbeil H, Harris A (2005) Lengths and hazards from channel-fed lava flows on Mauna  
483 Loa, Hawai'i, determined from thermal and downslope modeling with FLOWGO. *Bull. Volcanol.*,  
484 67, 634–647.

485 Stevens NF (2002) Emplacement of the large andesitic lava flow in the Oturere Stream valley,  
486 Tongariro Volcano, from airborne interferometric radar. *New Zealand Journal of Geology and*  
487 *Geophysics*, 45, 387-394.

488 Vicari A, Herault A, Del Negro C, Coltelli M, Marsella M, Proietti C (2007) Modeling of the 2001 lava  
489 flow at Etna volcano by a Cellular Automata approach. *Environmental Modelling and Software*,  
490 22, 1464-1471.

491 Vicari A, Ganci G, Behncke B, Cappello A, Neri M, Del Negro (2011) Near-real-time forecasting of lava  
492 flow hazards during the 12–13 January 2011 Etna eruption. *Geophysical Research Letters*, 38,  
493 L13317. <http://doi.org/10.1029/2011GL047545>

494 Villeneuve N, Neuville DR, Boivin P, Bachèlery P, Richet P (2008) Magma crystallization and viscosity:  
495 a study of molten basalts from the Piton de la Fournaise volcano (La Réunion island). *Chemical*  
496 *Geology*, 256, 242–251

497 Wright R, Rothery DA, Blake S, Pieri DC (2000) Visualizing active volcanism with high spatial  
498 resolution satellite data: the 1991–1993 eruption of Mount Etna. *Bull. Volcanol.*, 62, 256–265

499 Wright R, Carn SA, Flynn LP (2005) A satellite chronology of the May–June 2003 eruption of Anatahan  
500 volcano. *Journal of Volcanology and Geothermal Research*, 146, 102-116.

501 Wright R, Garbeil H, Harris AJL (2008) Using infrared satellite data to drive a  
502 thermorheological/stochastic lava flow emplacement model: A method for near-real-time  
503 volcanic hazard assessment. *Geophys Res Lett.*, 35(L19307). doi:10.1029/2008GL035228

504 Zakšek K, Hort M, Lorenz E (2015) Satellite and Ground Based Thermal Observation of the 2014  
505 Effusive Eruption at Stromboli Volcano. *Remote Sens.*, 7, 17190-17211.

506 Zebker HA, Rosen P, Hensley S, Mouginiis-Mark PJ (1996) Analysis of active lava flows on Kilauea  
507 volcano, Hawaii, using SIR-C radar correlation measurements. *Geology*, 24(6), 495-498.

508 Zhukov B, Lorenz E, Oertel D, Wooster M, Roberts G (2006) Spaceborne detection and  
509 characterization of fires during the bi-spectral infrared detection (BIRD) experimental small  
510 satellite mission (2001-2004). *Remote Sens. Environ.*, 100, 29–51

511 Young P, Wadge G (1990). FLOWFRONT: Simulation of a lava flow. *Computers and Geosciences*, 16,  
512 1171-1191.

513

514 **Figure Captions**

515 Figure 1. Location of the vent for the April–May 2018 eruption on the Dolomieu cone overlain on  
516 Google Earth with (a) MODIS, (b) ASTER and (c) thermal camera mosaic of the hot spots  
517 associated with active lava flow on 4 May overlain. Yellow outline in (c) gives the limit of the flow  
518 field as mapped using hand-held GPS.

519 Figure 2. Flow chart giving the call-down and reporting procedure, as well as flow of source terms,  
520 between each model.

521 Figure 3. DOWNFLOW inundation area for a 10000 iterations from the initial vent location with DEM  
522 noise (Dh) of 0.8 m (light blue) and 2.5 m (dark blue), with the line of steepest descent in red.  
523 Yellow stars give the distance down the LoSD FLOWGO runs at each generic effusion rate  
524 (numbers are in  $\text{m}^3/\text{s}$ ). These are the “effusion rate contours” for this eruption.

525 Figure 4. Distance down the LoSD (red line) that FLOWGO will run at the given effusion rates, these  
526 being the numbers (in  $\text{m}^3/\text{s}$ ) next to each star. Runs are given from (a) the initial vent location of  
527 28 April, and (b) the tube exit on 9 May. Overlain are the limits of the flow field defined from  
528 InSAR incoherence (blue outline) and field mapping (yellow outline) on the same dates.  
529 Background shows the DOWNFLOW inundation area.

530 Figure 5. Time-series of InSAR incoherence images with lava flow field outlined in blue.

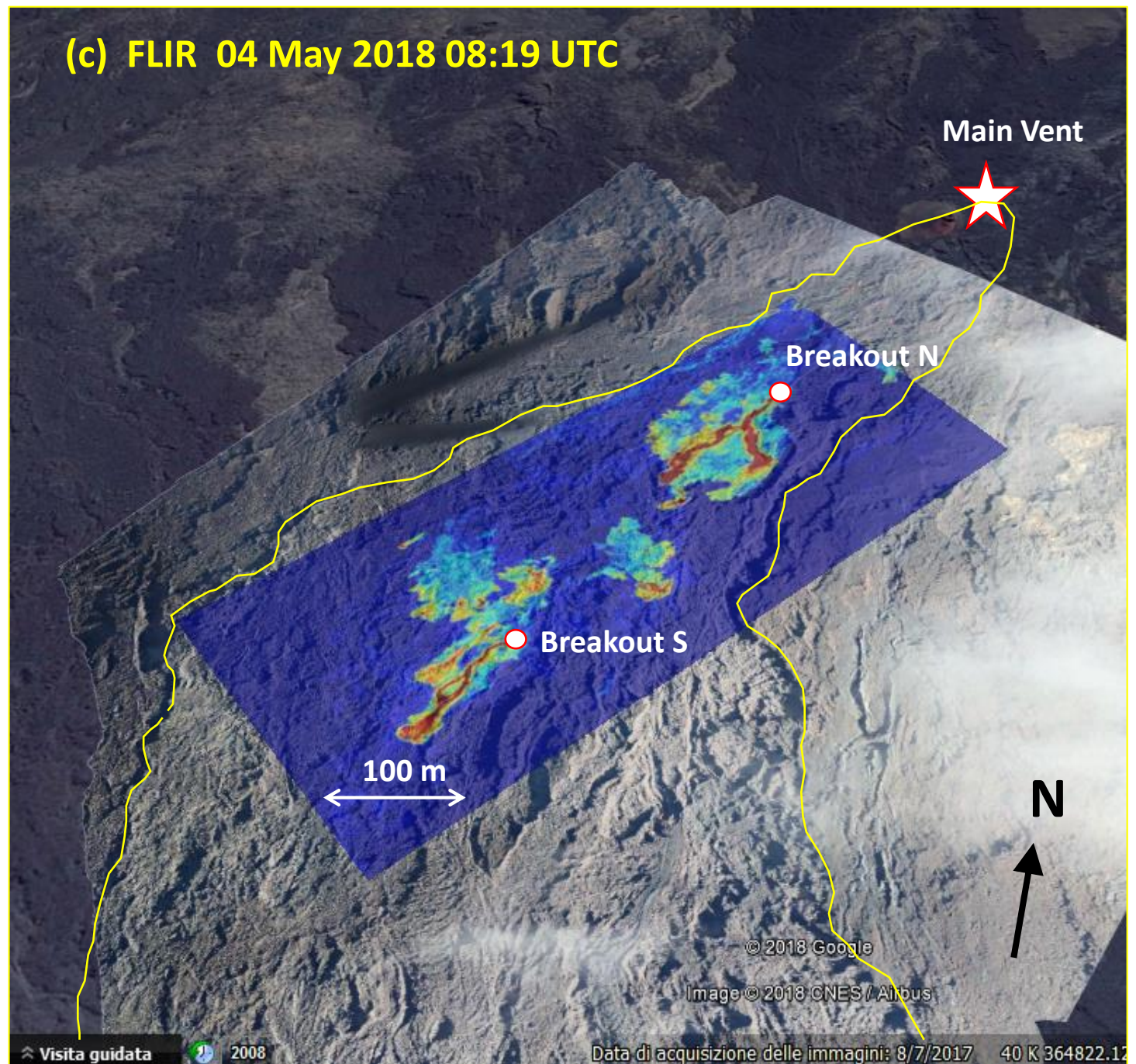
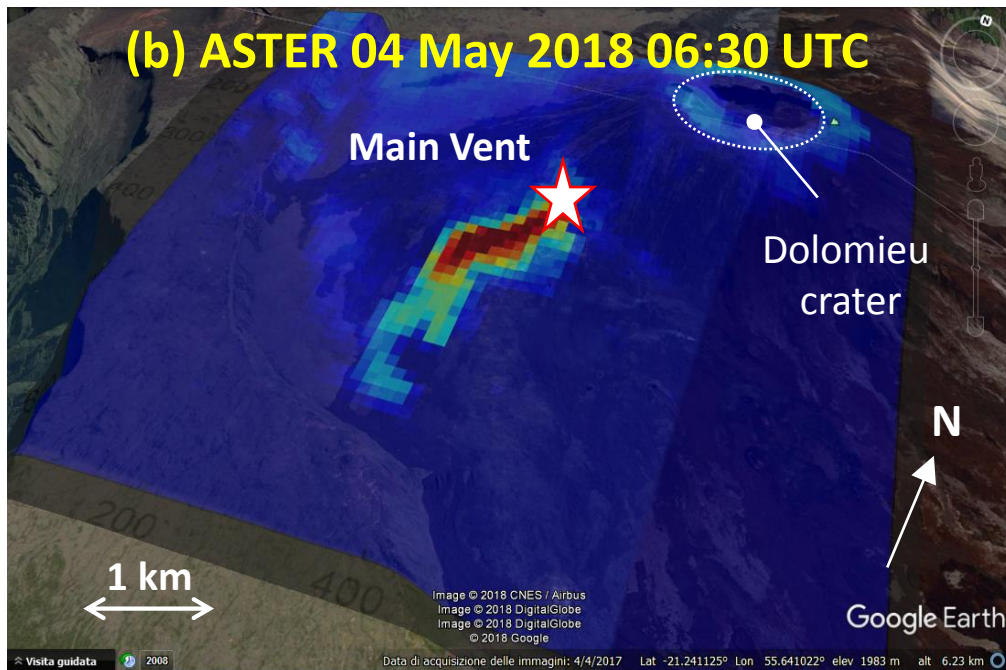
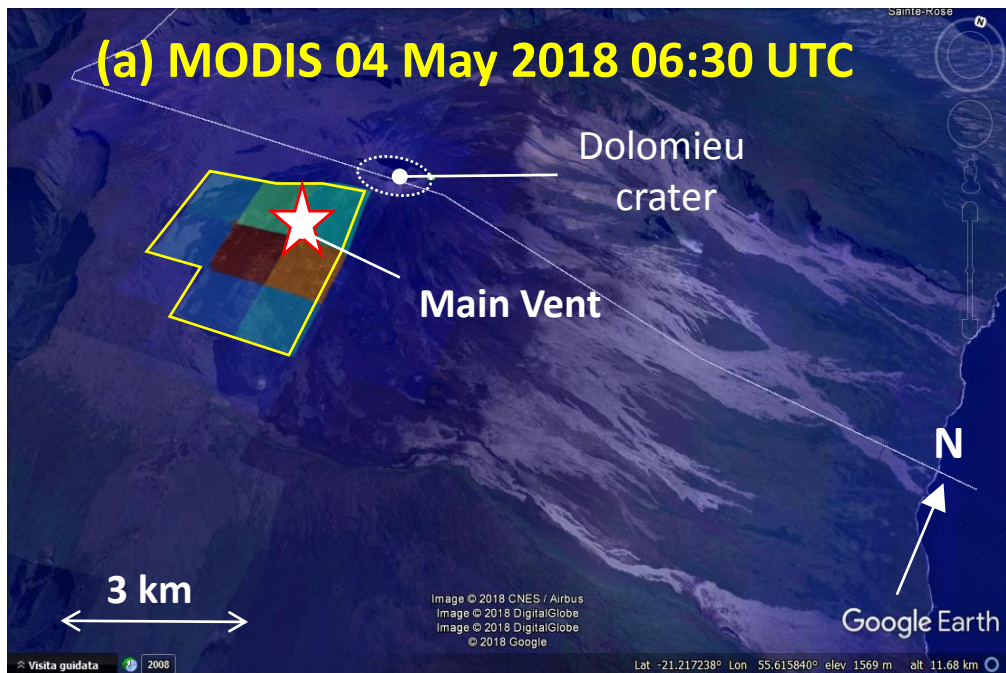
531 Figure 6. Time-series of ASTER TIR images with active flows apparent as elongate thermal anomalies  
532 (higher pixel-integrated temperatures give lighter tones: white are the hottest pixels, and black  
533 are the coldest). Note how the highest intensities in the thermal anomaly move down flow with  
534 time, and effect of lava tube extension.

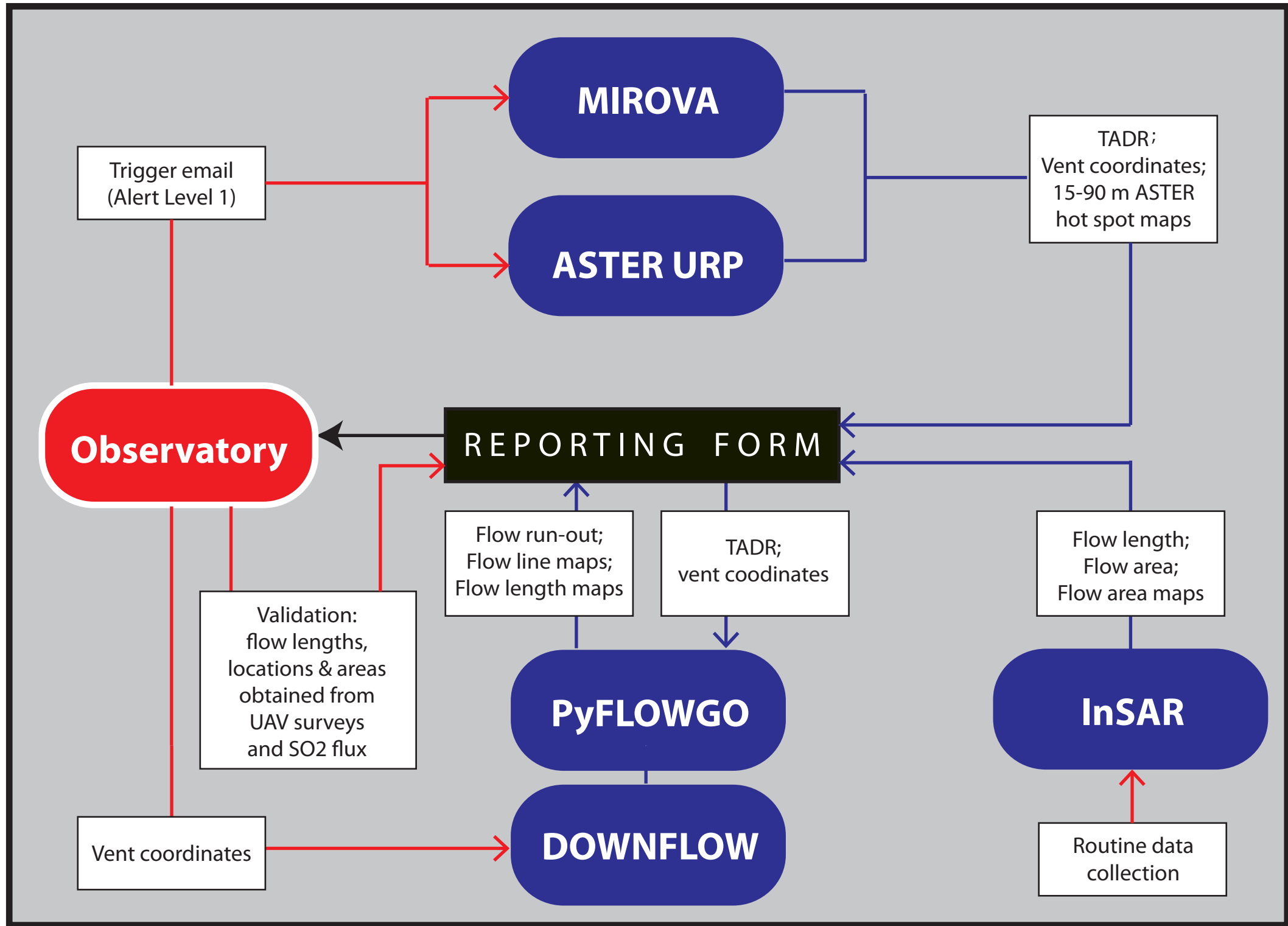
535 Figure 7. MIROVA-derived TADR and cumulative volume.

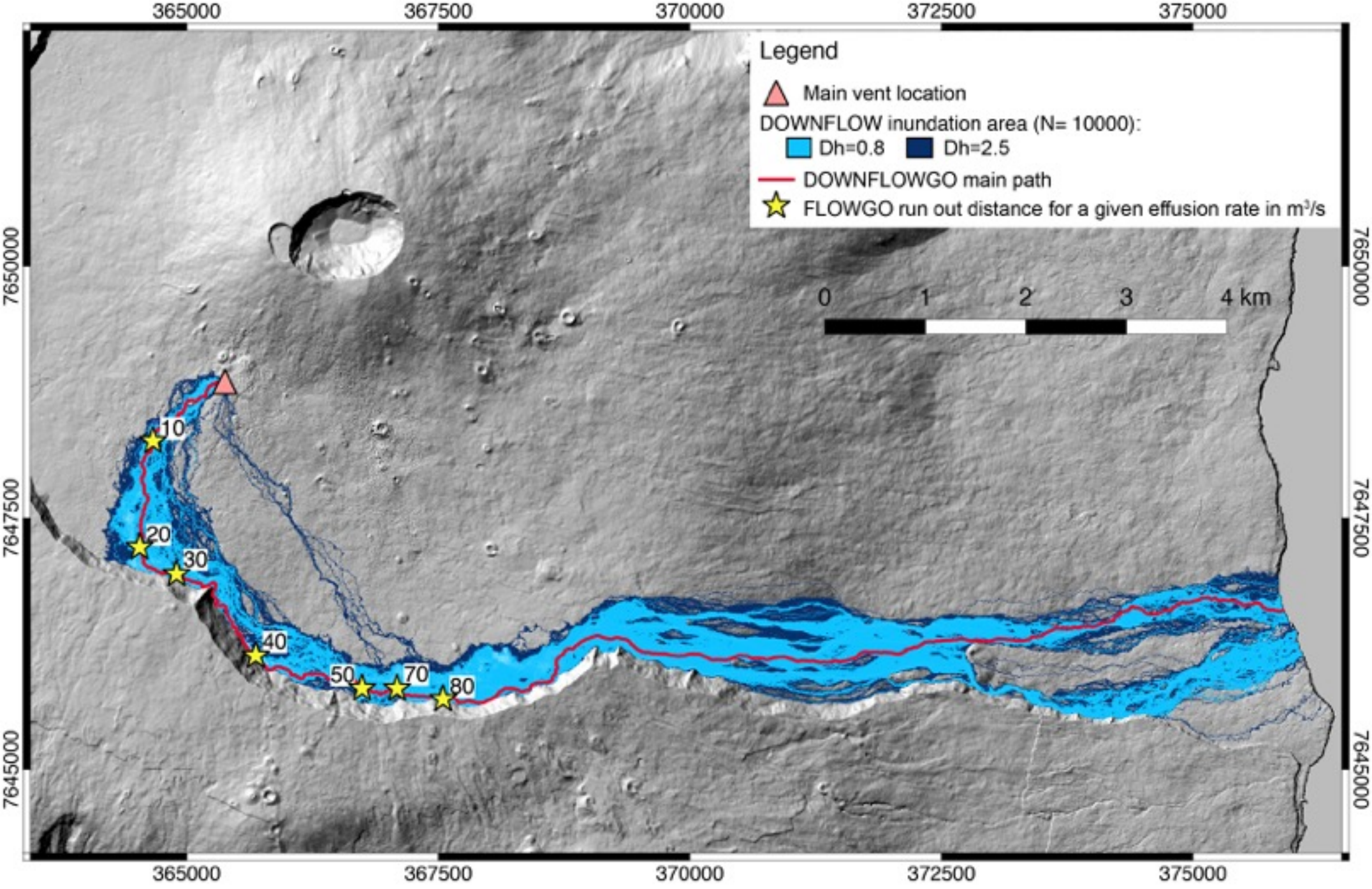
536 Figure 8. Comparison of ASTER thermal anomaly, InSAR incoherence and FLOWGO run outs for (a) 4  
537 May (FLOWGO run from the initial vent location) and (b) 9 May (FLOWGO run from the tube exit  
538 along the new path, yellow line).

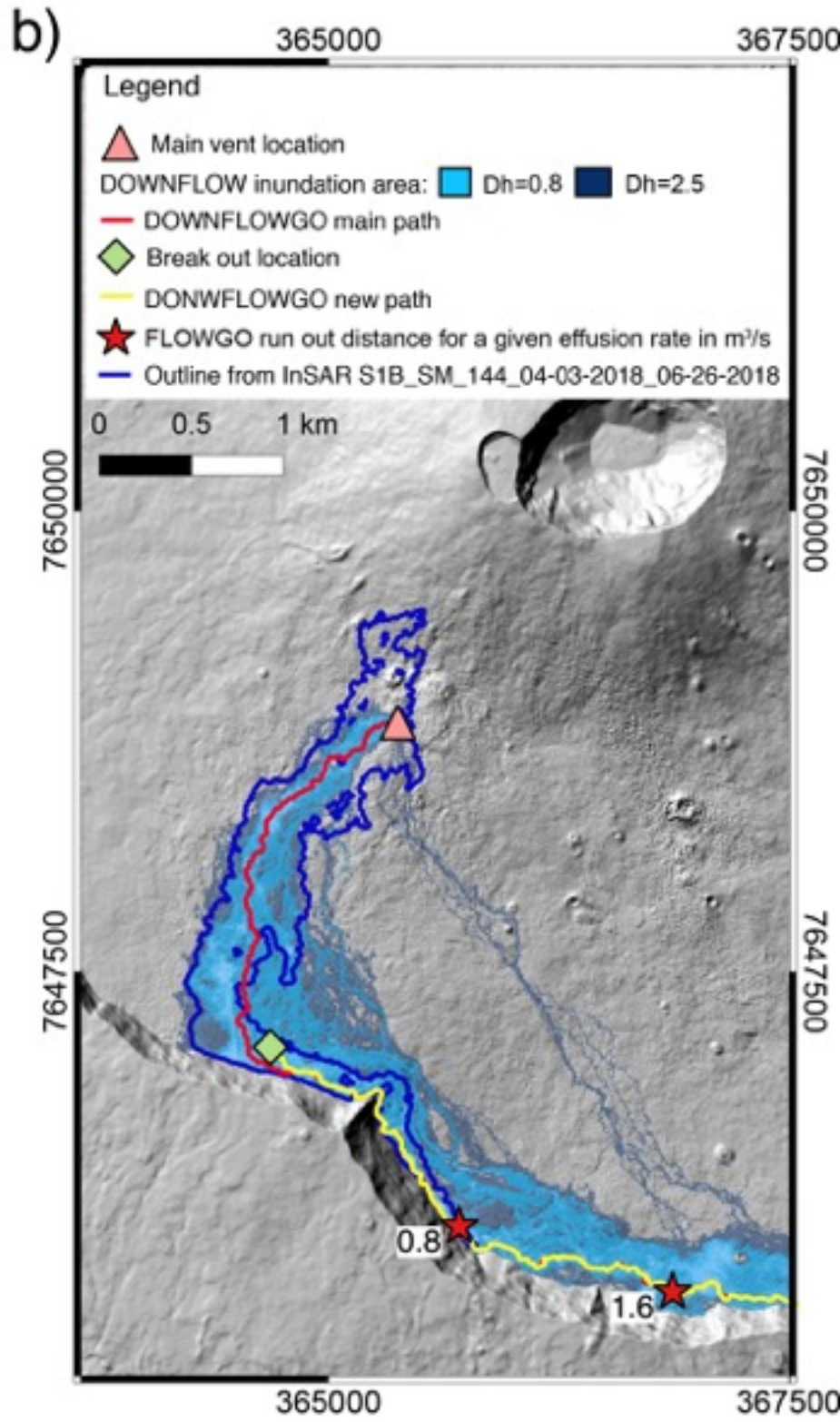
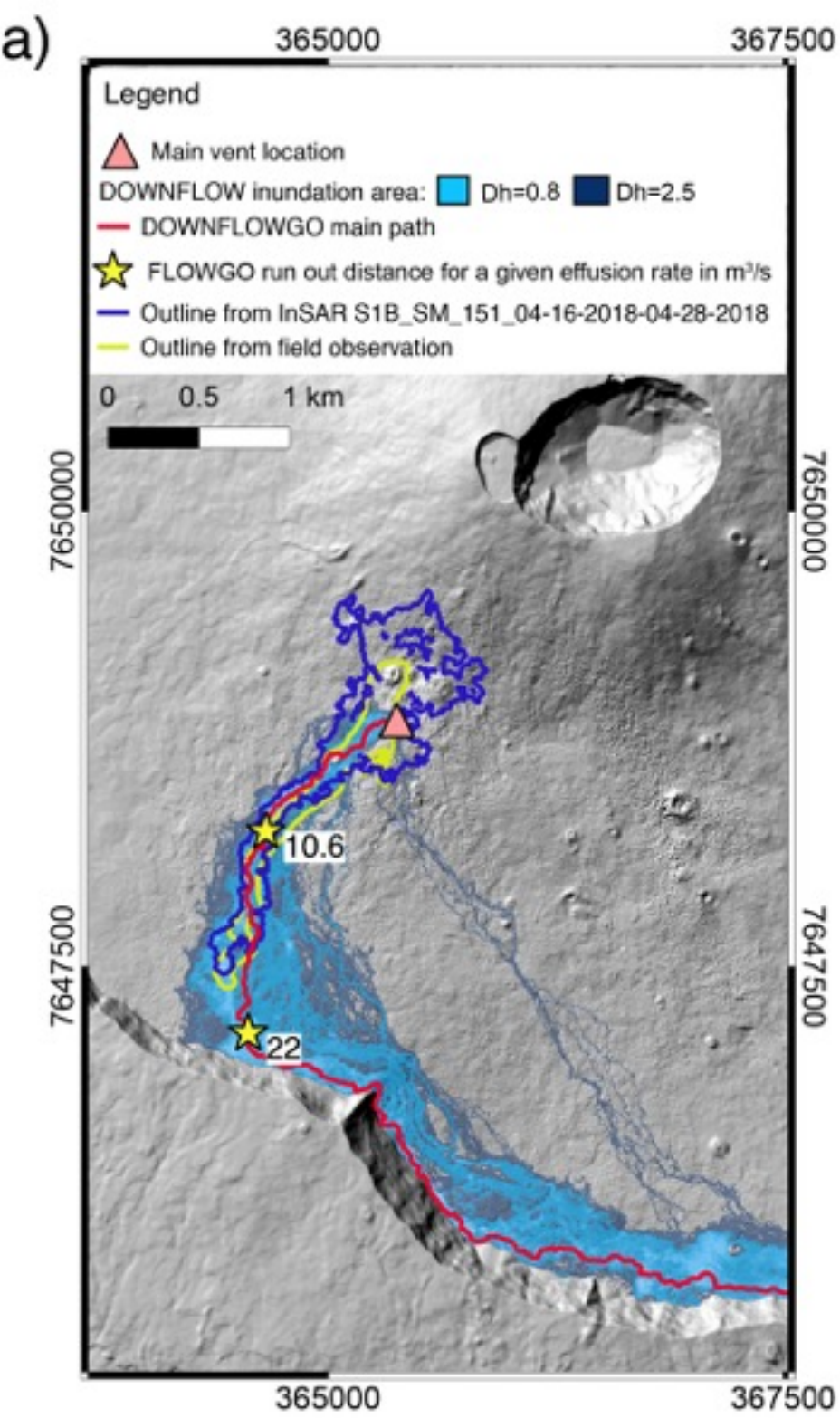
539

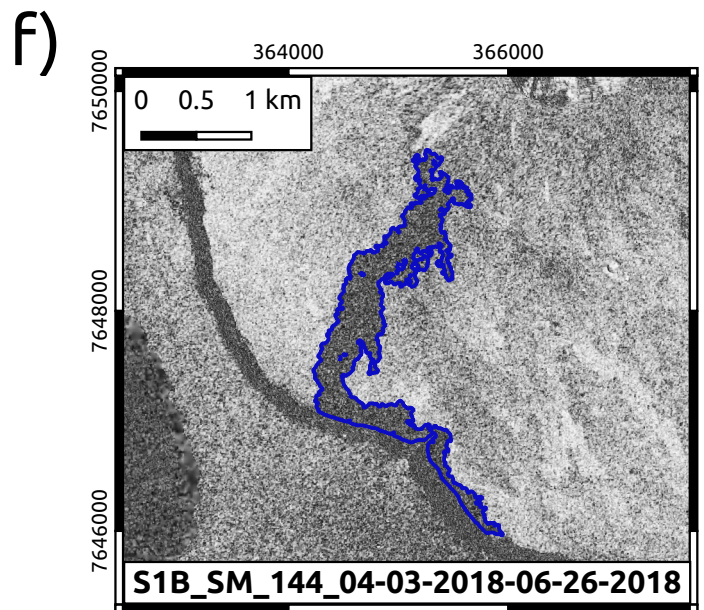
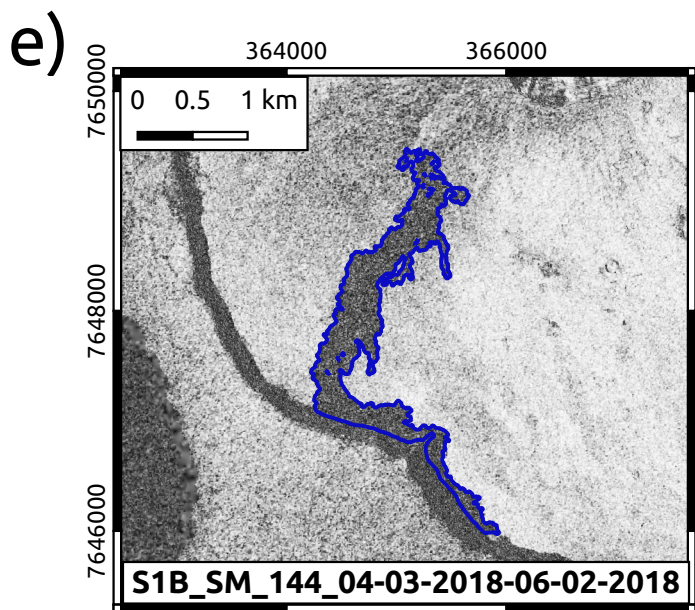
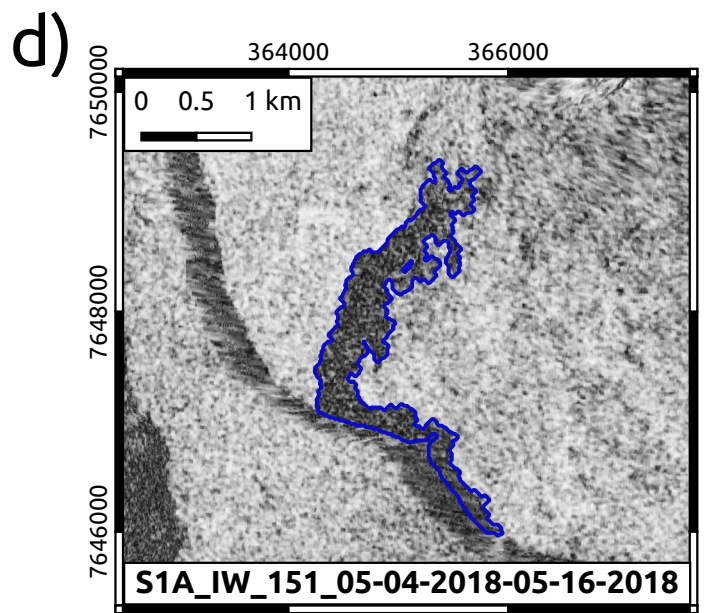
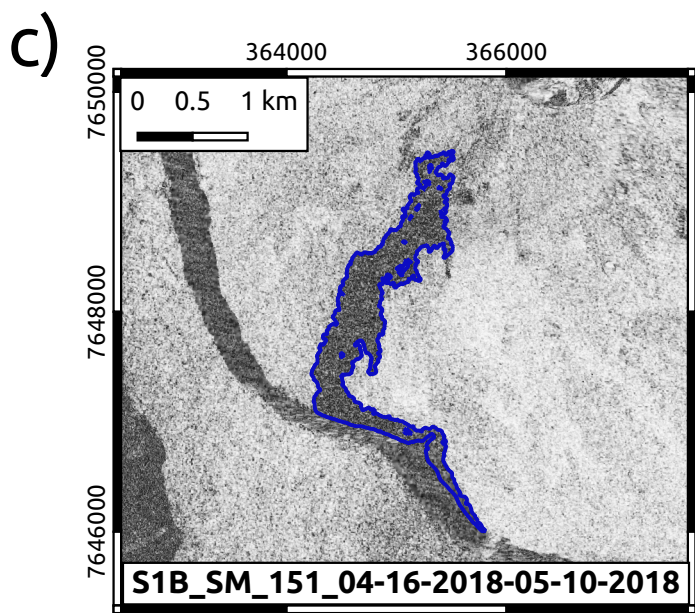
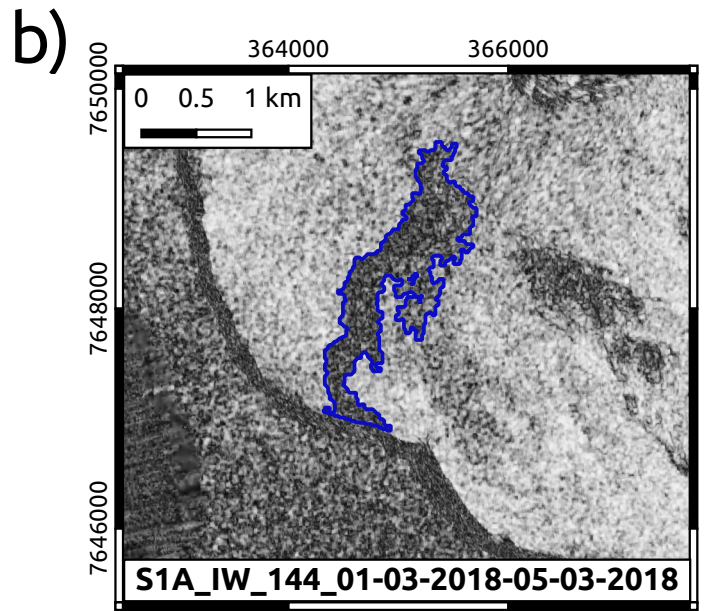
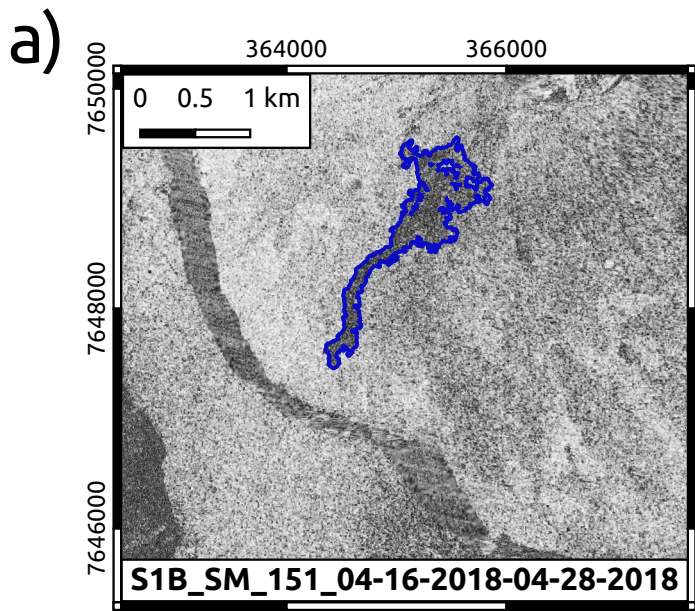






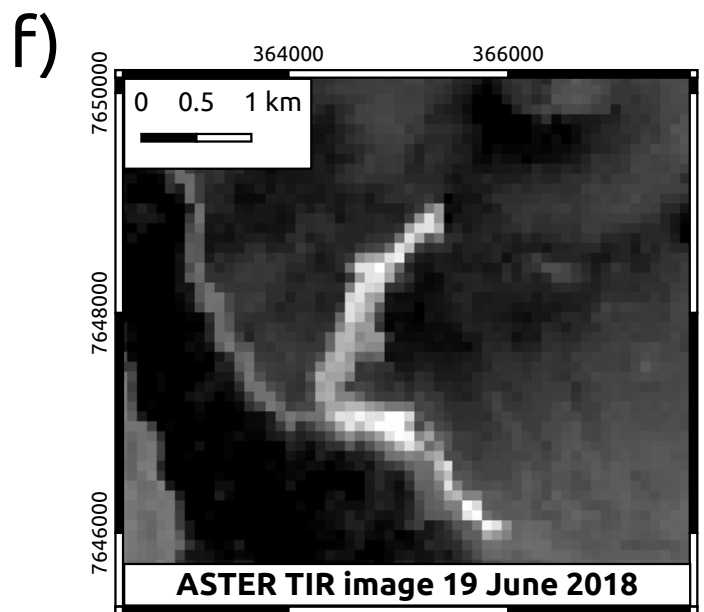
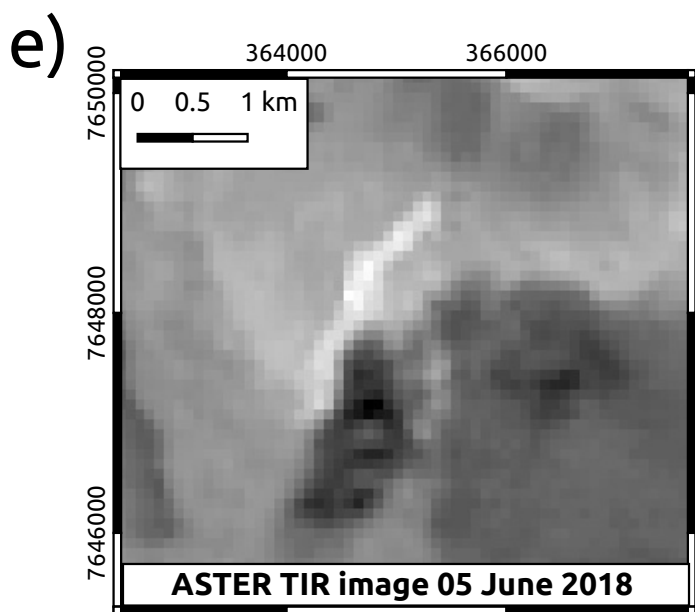
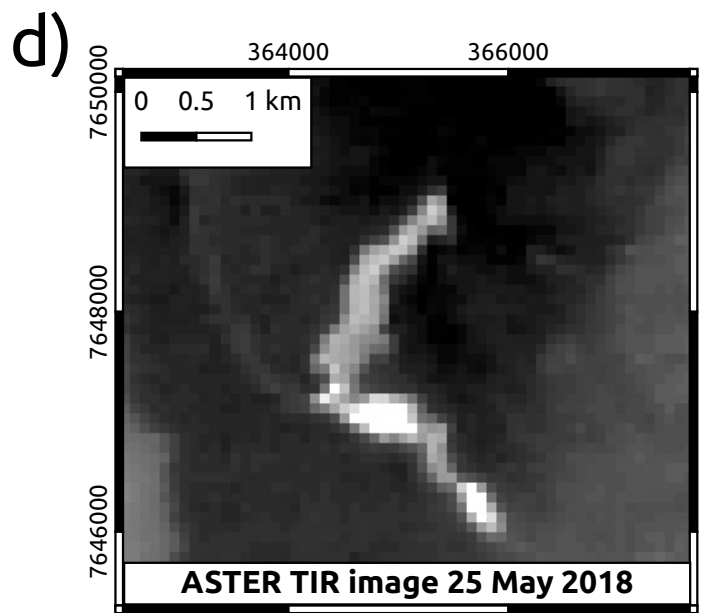
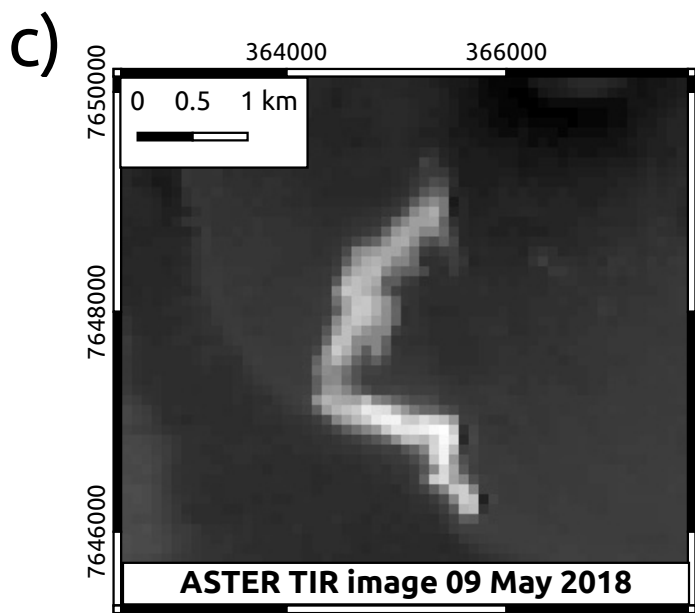
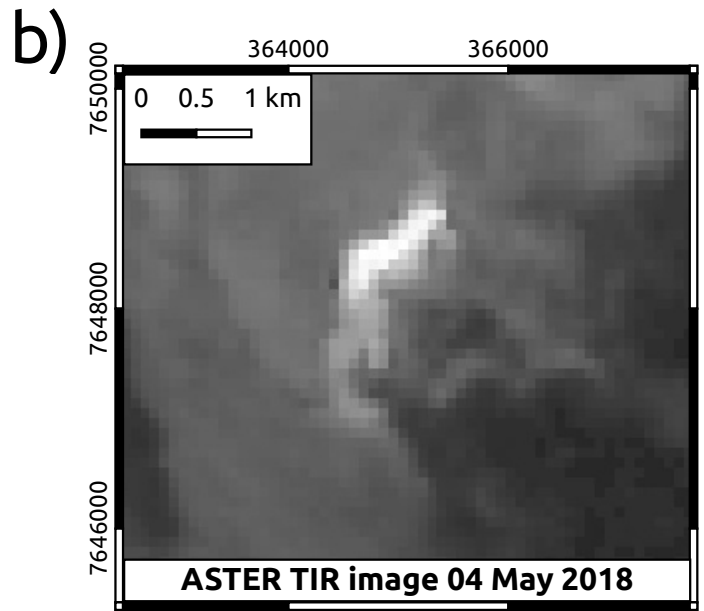
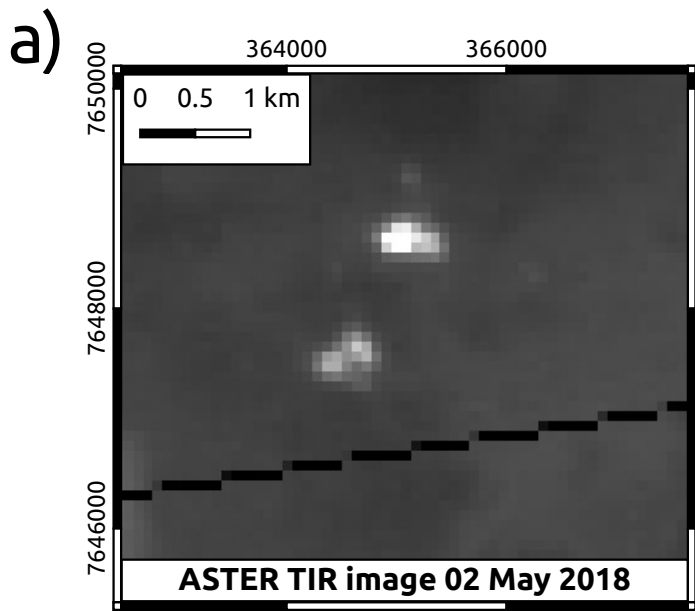






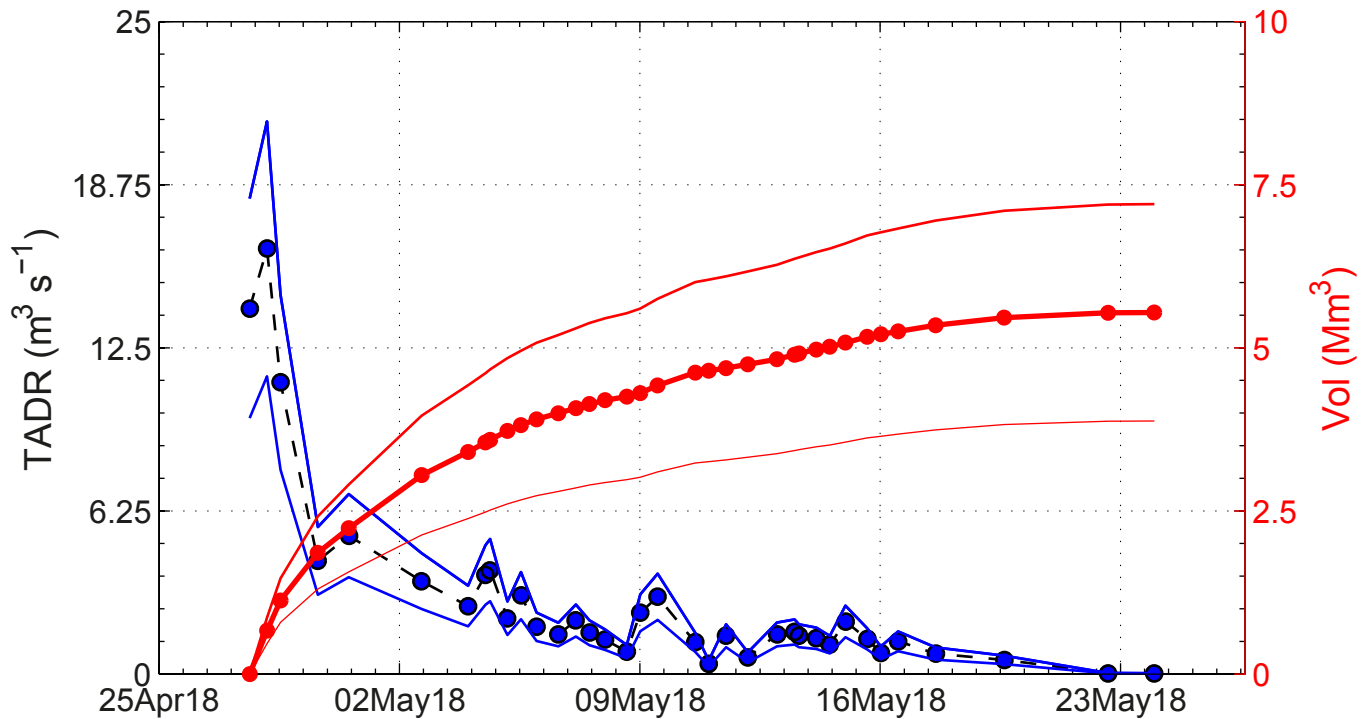
**Coherence**





**Temperature**





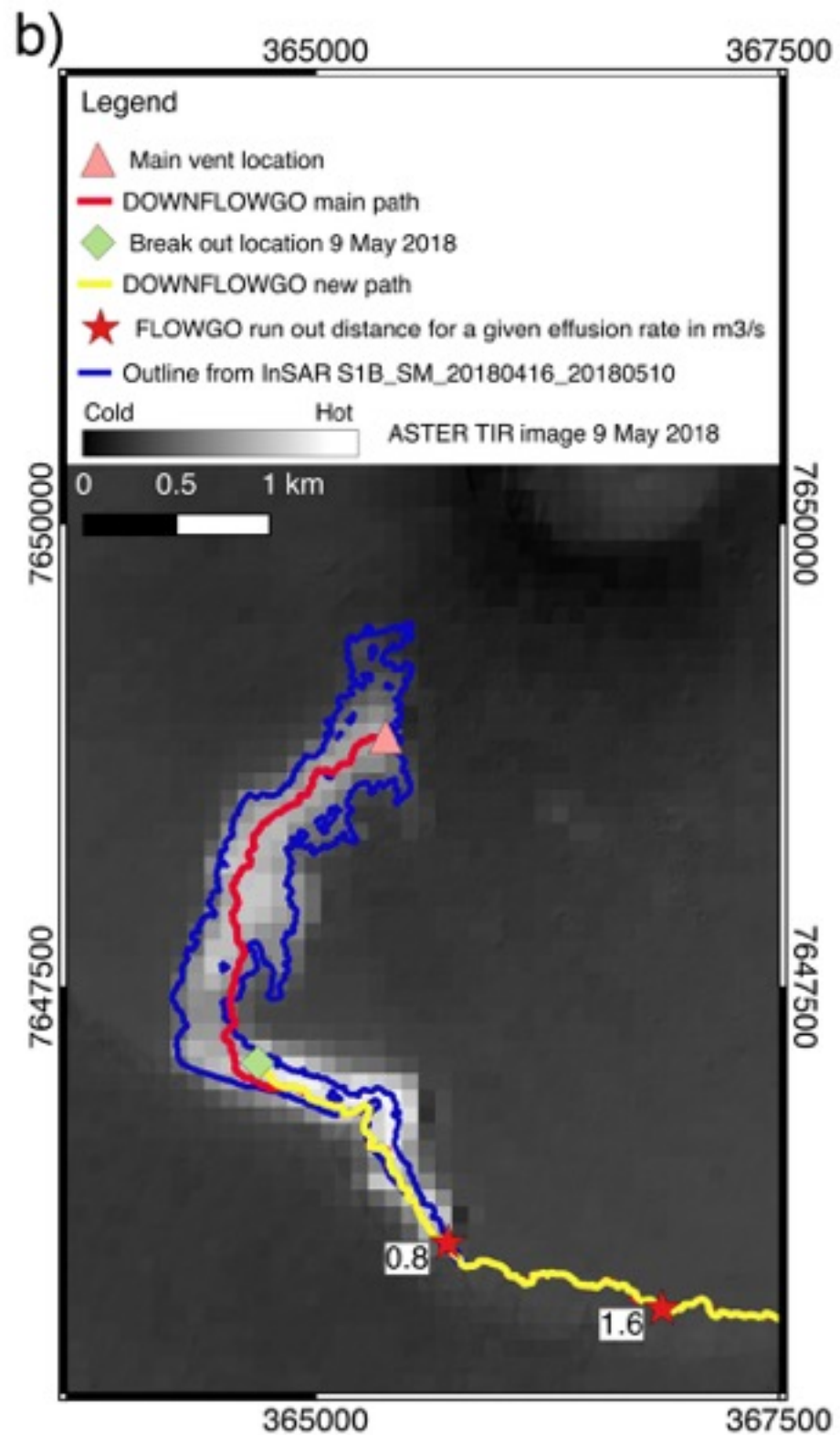
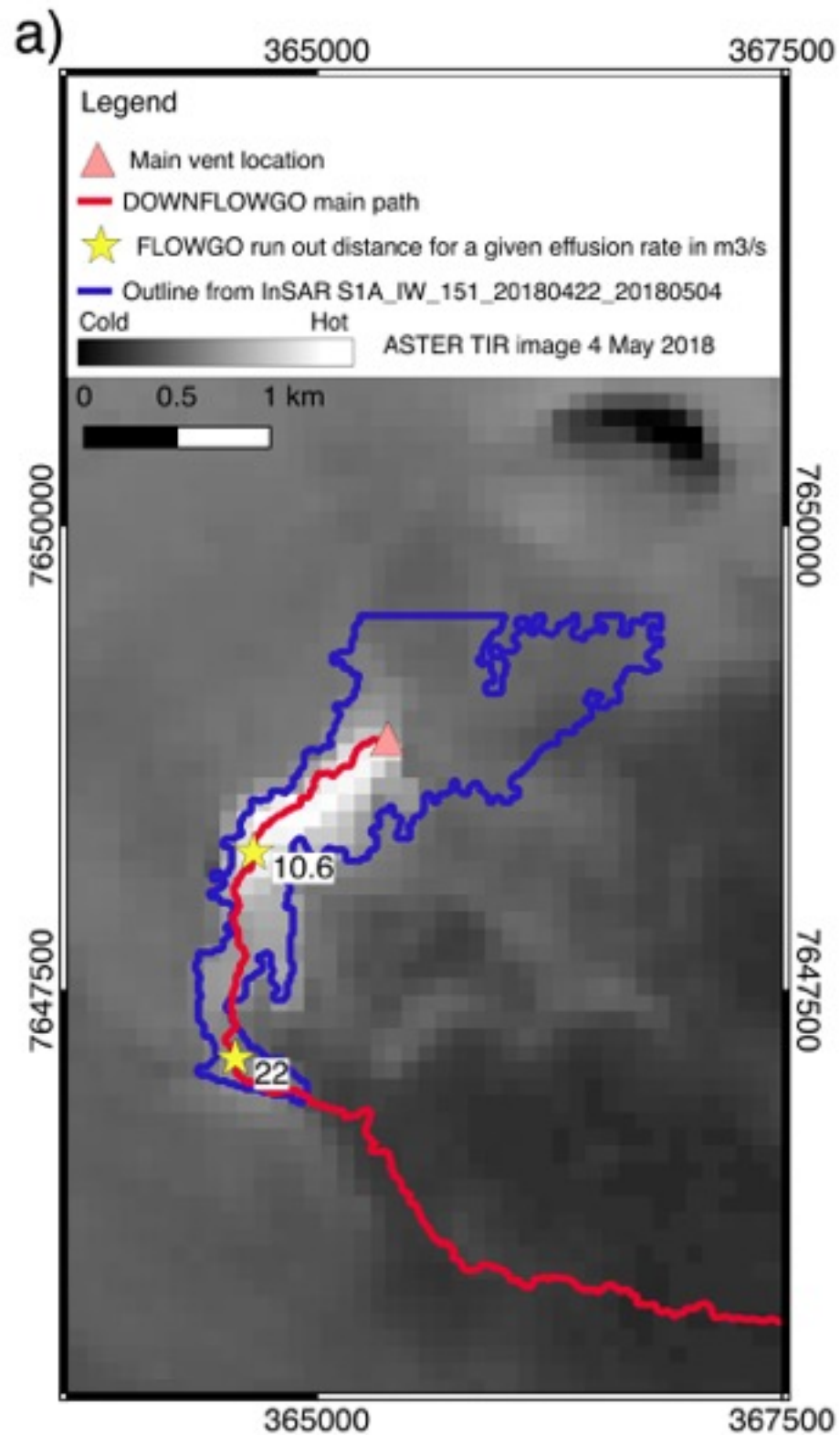




**Table 1.** Key thermal, textural and rheological source terms used to initialize PyFLOWGO at Piton de la Fournaise as given by Chevrel et al. (2018). These are based on measurements and best-fit testing of FLOWGO on lava channels active during the December 2010 eruption of Piton de la Fournaise as described in Harris et al. (2016).

Parameter	Value	Units	Up-dated value	Source
Channel width	4	m	2 m	Updated from channel dimensions on aerial photos of 4 May
Eruption Temperature	1114	°C	1140 °C	Updated from maximum temperature data from thermal imagery of the active vent on 4 May
Phenocryst content	0.10	volume fraction	0.01 vol.%	Minimum from the 2015 lava channel
Bubble content	0.30	volume fraction	0.5 vol.%	Maximum from the 2015 lava channel
DRE Density	2970	kg/m <sup>3</sup>		
Crust cover	100	%		
Effective Radiation Temperature	500	°C	740 °C	Mean temperature from thermal images of the south breakout channel on 4 May
Melt viscosity	Model of Villeneuve et al. (2008)	Pa s		Temperature dependent viscosity for a Piton de la Fournaise melt
Effect of crystals on mixture viscosity	Einstein Roscoe	Pa s		Valid for prolate crystal content < 0.1 (Mueller et al.2010)

**Table 2.** Cloud-free MODIS images processed and TADR delivered during the April-May 2018 eruption

Date & Time (UT) (dd/mm/yyyy hh:mm)	Satellite	TADR (m <sup>3</sup> /s)			Duration (days)	Cumulative Volume (× 10 <sup>6</sup> m <sup>3</sup> )		
		Min.	Mid-point	Max.		Min.	Mid-point	Max.
28/04/2018 09:55	<i>Aqua</i>	11.4	16.3	21.2	0.51	0.47	0.66	0.86
28/04/2018 19:20	<i>Terra</i>	7.8	11.2	14.5	0.90	0.79	1.13	1.47
29/04/2018 21:30	<i>Aqua</i>	3.0	4.3	5.6	1.99	1.30	1.86	2.42
30/04/2018 19:05	<i>Terra</i>	3.7	5.3	6.9	2.89	1.56	2.23	2.90
02/05/2018 22:00	<i>Aqua</i>	2.5	3.6	4.6	5.01	2.13	3.05	3.96
04/05/2018 06:30	<i>Terra</i>	1.8	2.6	3.4	6.36	2.38	3.41	4.43
04/05/2018 18:40	<i>Terra</i>	2.7	3.8	4.9	6.87	2.48	3.55	4.61
04/05/2018 21:50	<i>Aqua</i>	2.8	4.0	5.2	7.00	2.51	3.59	4.67
05/05/2018 10:00	<i>Aqua</i>	1.5	2.1	2.8	7.51	2.61	3.72	4.84
05/05/2018 19:25	<i>Terra</i>	2.1	3.0	3.9	7.90	2.67	3.81	4.95
06/05/2018 06:20	<i>Terra</i>	1.3	1.8	2.4	8.36	2.73	3.91	5.08
06/05/2018 21:35	<i>Aqua</i>	1.1	1.5	2.0	8.99	2.80	4.00	5.20
07/05/2018 09:45	<i>Aqua</i>	1.4	2.0	2.7	9.50	2.85	4.08	5.30
07/05/2018 19:15	<i>Terra</i>	1.1	1.6	2.1	9.90	2.90	4.14	5.38
08/05/2018 06:10	<i>Terra</i>	0.9	1.3	1.7	10.35	2.94	4.19	5.45
08/05/2018 21:25	<i>Aqua</i>	0.6	0.9	1.1	10.99	2.98	4.25	5.53
09/05/2018 06:50	<i>Terra</i>	1.6	2.3	3.1	11.38	3.02	4.31	5.60
09/05/2018 19:00	<i>Terra</i>	2.1	3.0	3.8	11.89	3.10	4.42	5.75
10/05/2018 21:15	<i>Aqua</i>	0.9	1.2	1.6	12.98	3.23	4.62	6.01
11/05/2018 06:40	<i>Terra</i>	0.3	0.4	0.5	13.37	3.25	4.65	6.04
11/05/2018 18:50	<i>Terra</i>	1.0	1.5	1.9	13.88	3.28	4.69	6.10
12/05/2018 10:05	<i>Aqua</i>	0.4	0.6	0.8	14.51	3.32	4.75	6.17
13/05/2018 06:25	<i>Terra</i>	1.1	1.5	2.0	15.36	3.38	4.83	6.27
13/05/2018 18:35	<i>Terra</i>	1.1	1.6	2.1	15.87	3.43	4.89	6.36
13/05/2018 21:45	<i>Aqua</i>	1.0	1.5	1.9	16.00	3.44	4.91	6.39
14/05/2018 09:55	<i>Aqua</i>	1.0	1.4	1.8	16.51	3.48	4.97	6.47

14/05/2018 19:20	<i>Terra</i>	0.8	1.1	1.5	16.90	3.51	5.02	6.52
15/05/2018 06:15	<i>Terra</i>	1.4	2.0	2.6	17.35	3.55	5.08	6.60
15/05/2018 21:30	<i>Aqua</i>	0.9	1.3	1.7	17.99	3.62	5.17	6.72
16/05/2018 06:55	<i>Terra</i>	0.6	0.8	1.1	18.38	3.64	5.21	6.77
16/05/2018 19:05	<i>Terra</i>	0.9	1.3	1.6	18.89	3.68	5.25	6.83
17/05/2018 21:20	<i>Aqua</i>	0.5	0.8	1.0	19.98	3.74	5.35	6.95
19/05/2018 21:05	<i>Aqua</i>	0.4	0.5	0.7	21.97	3.82	5.46	7.10
22/05/2018 21:35	<i>Aqua</i>	0.02	0.03	0.04	24.99	3.88	5.54	7.20
24/05/2018 06:10	<i>Terra</i>	0.02	0.02	0.03	26.35	3.88	5.54	7.20

---

Table 3. InSAR image pairs used to produce coherence maps during the April – May eruption, and the resulting flow lengths and flow field areas. The lines entered in bold are used in the reporting form (Appendix A). Track 144 for ascending pass; 151 for descending pass.

Satellite	Mode (track)	Date (dd/mm/yyyy)		Time (UT) (hh:mm:ss)	Length (km)	Area (x 10 <sup>6</sup> m <sup>2</sup> )	Error (x 10 <sup>6</sup> m <sup>2</sup> )
		Master	Slave				
<b>S1B</b>	<b>SM (151)</b>	<b>16/04/2018</b>	<b>28/04/2018</b>	<b>01:46:38</b>	<b>1.8</b>	<b>0.5</b>	<b>0.1</b>
<b>S1A</b>	<b>IW (144)</b>	<b>03/01/2018</b>	<b>03/05/2018</b>	<b>14:53:11</b>	<b>2.5</b>	<b>1.0</b>	<b>0.3</b>
S1A	IW (151)	22/04/2018	04/05/2018	01:47:32	2.6	--	--
S1B	SM (144)	27/04/2018	09/05/2018	14:52:40	3.4	1.1	0.1
<b>S1B</b>	<b>SM (151)</b>	<b>16/04/2018</b>	<b>10/05/2018</b>	<b>01:46:39</b>	<b>3.5</b>	<b>1.2</b>	<b>0.2</b>
S1A	IW (144)	03/01/2018	15/05/2018	14:53:12	4.0	1.2	0.2
<b>S1A</b>	<b>IW (151)</b>	<b>04/05/2018</b>	<b>16/05/2018</b>	<b>01:47:32</b>	<b>4.1</b>	<b>1.3</b>	<b>0.3</b>
S1B	SM (144)	27/04/2018	21/05/2018	14:52:41	4.1	--	--
S1B	SM (151)	16/04/2018	22/05/2018	01:46:39	4.1	1.3	0.1
S1A	IW (144)	03/01/2018	27/05/2018	14:53:12	4.1	1.3	0.1
S1A	IW (151)	04/05/2018	28/05/2018	01:47:33	4.1	1.3	0.1
S1B	SM (144)	27/04/2018	02/06/2018	14:52:41	--	--	--
S1B	SM (151)	16/04/2018	03/06/2018	01:46:40	--	--	--
S1A	IW (144)	03/01/2018	08/06/2018	14:53:13	4.1	--	--
S1A	IW (151)	04/05/2018	09/06/2018	01:47:34	4.1	--	--

**Table 4.** ASTER-URP images acquired during the eruption response. From these data, vent locations and flow field lengths were derived. Note that when the 15 m VNIR are the only data acquired because of high angle off-nadir pointing, smaller-scale features are resolved, but the dimensions of active flow features based on their thermal signature cannot be measured without the 90 m TIR data.

Date (dd/mm/yyyy)	Time (hh:mm, UT)	Mode	Vent Location (UTM)	Tube Exit Location (UTM)	Tube length (km)	Active flow length (km)	Cooling flow length (km)
02/05/2018	18:56	Night time mode (TIR only)	0365216 m E; 7648811 m S	n/a	0	0.99	1.53
04/05/2018	06:34	Daytime full mode (both VNIR and TIR)	0365261 m E; 7648841 m S	n/a	0	0.89	1.33
09/05/2018	19:03	Night time mode (TIR only)	0365261 m E; 7648841 m S	0364927 m E; 7646953 m S	0.49	1.52	1.67
11/05/2018	6:40	Daytime off-nadir pointing mode (VNIR only)	--	--	--	--	--
13/05/2018	6:28	Daytime off-nadir pointing mode (VNIR only)	--	--	--	--	--
18/05/2018	18:57	Night time mode (TIR only)	cloudy	cloudy	cloudy	cloudy	cloudy
20/05/2018	06:34	Daytime full mode (both VNIR and TIR)	cloudy	cloudy	cloudy	cloudy	cloudy
25/05/2018	19:03	Night time mode (TIR only)	0365261 m E; 7648841 m S	0364900 m E; 7647010 m S	2.07	0.63	1.08
03/06/2018	18:57	Night time mode (TIR only)	cloudy	cloudy	cloudy	cloudy	cloudy
05/06/2018	06:34	Daytime full mode (both VNIR and TIR)	Post-eruption	Post-eruption	Post-eruption	Post-eruption	Post-eruption
19/06/2018	18:57	Night time mode (TIR only)	Post-eruption	Post-eruption	Post-eruption	Post-eruption	Post-eruption

**LAVA FLOW FIELD REPORTING FORM**  
 (file name save format: yyyyymmdd-Volcano name-ANR-LAVA-REPORT-##)

Target	<VOLCANO NAME>
Eruption Start Date and Time (local)	<yyyy-mm-dd-T-hh-mm> (local time)
Report Initialization Date and Time (UTC)	<yyyy-mm-dd-T-hh-mm> (GMT)
Reporting form initialized by	<SURNAME> <name>

**Field 1: TIME-AVERAGED DISCHARGE RATE**

Sensor	<Sensor name>
Processing System	<Hot spot detection system>
Last update	<yyyy-mm-dd-T-hh-mm>
Up-dated by	<SURNAME> <name>

Image Date	Image Time	TADR-min	TADR-max
<yyyy-mm-dd>	<hh-mm>	<m <sup>3</sup> /s>	<m <sup>3</sup> /s>
<yyyy-mm-dd>	<hh-mm>	<m <sup>3</sup> /s>	<m <sup>3</sup> /s>
<yyyy-mm-dd>	<hh-mm>	<m <sup>3</sup> /s>	<m <sup>3</sup> /s>
<yyyy-mm-dd>	<hh-mm>	<m <sup>3</sup> /s>	<m <sup>3</sup> /s>
<yyyy-mm-dd>	<hh-mm>	<m <sup>3</sup> /s>	<m <sup>3</sup> /s>
<yyyy-mm-dd>	<hh-mm>	<m <sup>3</sup> /s>	<m <sup>3</sup> /s>
<yyyy-mm-dd>	<hh-mm>	<m <sup>3</sup> /s>	<m <sup>3</sup> /s>
<yyyy-mm-dd>	<hh-mm>	<m <sup>3</sup> /s>	<m <sup>3</sup> /s>
<yyyy-mm-dd>	<hh-mm>	<m <sup>3</sup> /s>	<m <sup>3</sup> /s>
<yyyy-mm-dd>	<hh-mm>	<m <sup>3</sup> /s>	<m <sup>3</sup> /s>

**Comments:**

<free text>

**Time Series:**

Start date	Current date	No. data points	Duration
<yyyy-mm-dd>	<yyyy-mm-dd>	<##>	<days>

<place time-series graph here>  
 Y1-axis = "TADR (m<sup>3</sup>/s); Y2-axis = "Volume (× 10<sup>6</sup> m<sup>3</sup>)"; x-axis "Date (mm-dd)"

## Field 2: FLOW SIMULATION

Last update		<yyyy-mm-dd-T-hh-mm>	
Up-dated by		<SURNAME> <name>	
Flow path model		<model name>	
DEM date	DEM resolution	Noise	No. iterations
<yyyy-mm-dd>	<m>	<±m>	<##>
Vent location	Source: airborne GPS	Source: field GPS	Source: ASTER
<UTM>	<Y/N>	<Y/N>	<Y/N>
<GOOGLE?>	<yyyy-mm-dd>	<hh-mm> (local time)	
Flow length model		<model name>	
Initialization file		<file name>	
Run Date	TADR used	Channel dimension	Run out
<yyyy-mm-dd>	<m <sup>3</sup> /s>	<m>	<m>
<yyyy-mm-dd>	<m <sup>3</sup> /s>	<m>	<m>
<yyyy-mm-dd>	<m <sup>3</sup> /s>	<m>	<m>
<yyyy-mm-dd>	<m <sup>3</sup> /s>	<m>	<m>
<yyyy-mm-dd>	<m <sup>3</sup> /s>	<m>	<m>
<yyyy-mm-dd>	<m <sup>3</sup> /s>	<m>	<m>
<yyyy-mm-dd>	<m <sup>3</sup> /s>	<m>	<m>
Flow projection map:			
Vent position	Current run date	TADR used	Eruption temperature
<UTM>	<yyyy-mm-dd>	<m <sup>3</sup> /s>	<°C>
<place PYFLOWGO output here> PYFLOWGO parameter output screen		<place map output here> DOWNFLOW paths with FLOWGO distances on shaded relief	
<b>Comments:</b>			
<free text>			

### Field 3: ASTER

Last update		<yyyy-mm-dd-T-hh-mm>	
Up-dated by		<SURNAME> <name>	
Image date	Image time (UT)	TADR	SO <sub>2</sub> flux
<yyyy-mm-dd>	<hh-mm>	<m <sup>3</sup> /s>	<kg/s>
<yyyy-mm-dd>	<hh-mm>	<m <sup>3</sup> /s>	<kg/s>
<yyyy-mm-dd>	<hh-mm>	<m <sup>3</sup> /s>	<kg/s>
<yyyy-mm-dd>	<hh-mm>	<m <sup>3</sup> /s>	<kg/s>
Image date	Image time (UT)	Anomaly Length	Anomaly Area
<yyyy-mm-dd>	<hh-mm>	<m>	<m <sup>2</sup> >
<yyyy-mm-dd>	<hh-mm>	<m>	<m <sup>2</sup> >
<yyyy-mm-dd>	<hh-mm>	<m>	<m <sup>2</sup> >
<yyyy-mm-dd>	<hh-mm>	<m>	<m <sup>2</sup> >
ASTER hot spot map:			
Image date	Image time (UT)	VNIR bands used	TIR bands used
<yyyy-mm-dd>	<hh-mm>	<b#; b#; b#>	<b#; b#; b#>
<ASTER VNIR image> contrast enhanced, density sliced ASTER image on Google Earth		<ASTER TIR image> contrast enhanced, density sliced ASTER image on Google Earth	
<b>Comments:</b>			
<free text>			



### Field 4: INSAR

Last update		<yyyy-mm-dd-T-hh-mm>		
Up-dated by		<SURNAME> <name>		
Processing System		<InSAR processing system>		
	Satellite	Mode	Date	time
Master	<sat>	<mode>	<yyyy-mm-dd>	<hh-mm>
Slave	<sat>	<mode>	<yyyy-mm-dd>	<hh-mm>
Dimensions:	Length =	<m>	Area =	<m <sup>2</sup> >
Master	<sat>	<mode>	<yyyy-mm-dd>	<hh-mm>
Slave	<sat>	<mode>	<yyyy-mm-dd>	<hh-mm>
Dimensions:	Length =	<m>	Area =	<m <sup>2</sup> >
Master	<sat>	<mode>	<yyyy-mm-dd>	<hh-mm>
Slave	<sat>	<mode>	<yyyy-mm-dd>	<hh-mm>
Dimensions:	Length =	<m>	Area =	<m <sup>2</sup> >
Master	<sat>	<mode>	<yyyy-mm-dd>	<hh-mm>
Slave	<sat>	<mode>	<yyyy-mm-dd>	<hh-mm>
Dimensions:	Length =	<m>	Area =	<m <sup>2</sup> >
InSAR coherence and flow area maps:				
	Satellite	Mode	Date	time
Master	<sat>	<mode>	<yyyy-mm-dd>	<hh-mm>
Slave	<sat>	<mode>	<yyyy-mm-dd>	<hh-mm>
< coherence image >		<lava flow outline and length path>		
<b>Comments:</b>				
<free text>				

## Appendix B

### InSAR data processing

The InSAR method consists of computing an interferogram by subtracting the phase between two SAR images acquired of the same area at different epochs. The phase recorded on a SAR image depends both on the radar wave round trip travel time between the instrument and the ground, and on the interaction between the radar wave and reflectors on the ground surface. Provided that this last component remains stable between two successive acquisitions, the differential phase displayed on the interferogram will only reflect changes in the radar wave travel time between the two acquisitions and can be exploited to measure possible ground surface displacement occurring between the two acquisitions. This is the classical application of InSAR that has seen a successful development in the field of volcanological application since the pioneering work of Massonnet et al. (1995) (e.g., Biggs and Pritchard 2017; Pinel, Poland, and Hooper 2014; Massonnet, Briole, and Arnaud 1995; Ferretti, Prati, and Rocca 2001; Hooper et al. 2004).

If the geometry or dielectrical properties of the reflectors on the ground change significantly between the two radar acquisitions, the differential phase will appear very noisy (“decorrelated” or “incoherent”) on the interferogram, making it unexploitable for displacement measurement. This generally occurs when the ground is covered by dense vegetation, the geometric properties of individual plants changing very quickly due to continuous growth or to the motion of leaves in the wind. It could also occur when heavy rain, snow fall, strong erosional events, air fall (in volcanic context) occurs between the two radar acquisitions. Interferometric coherence provides an estimation of the temporal stability of the ground contribution to phase measurement. It is generally derived as an inverse function of the phase variance calculated between neighboring pixels (e.g., in a  $3 \times 3$  pixels box) in the interferogram and is usually represented as an image where very coherent pixels have values close to one and poorly coherent pixels have values close to zero.

If a lava flow is emplaced between two successive SAR acquisitions, the interferometric coherence will be very low in the area covered by the lava flow due to the change in the geometry of the ground reflectors there. If, in contrast, the surrounding area remains coherent on the interferogram (i.e., if the lava flow is emplaced on bare rock or soil), the lava flow will appear on the interferometric coherence image as a black area surrounded by lighter-toned pixels. This is typically the case at Piton de la Fournaise when a lava flow is emplaced in the (largely) vegetation-free Enclos Fouqué caldera (the upper part of the volcano) where the interferometric coherence is very high (>70 %). Here, by detecting the boundary between dark and light-toned areas one can obtain a map of the lava flow contour (e.g., Rowland et al. 2003; Dietterich et al. 2012; Bato et al. 2016).

In this study, we exploited interferometric coherence images to produce an early map of the April-May 2018 lava flow. To provide relevant data for input in the response protocol in as timely fashion as possible, we used only ESA Sentinel-1 data. Sentinel-1A/B data are acquired for La Réunion island every six days both during ascending and descending passes, alternatively in Interferometric Wide Swath mode (IW, range spacing = 2.33 m, azimuth spacing = 14.06 m) and in Stripmap mode (SM, range spacing = 2.66 m, azimuth spacing = 4.15 m). The data are made freely available by the European Space Agency (ESA) via the Sentinel-1 Data Hub between 4 and 24 hours after acquisition.

As it is not possible to produce an interferogram by combining IW with SM data, so the shortest time period between two usable interferograms is 12 days. We compute the interferograms and the coherence images using the Doris 5.0.3 InSAR processor (Kampes and Usai 1999; Kampes and Hanssen 2003). To georeference the interferometric products, we used a 5 m resolution Digital Elevation Model (DEM) produced by the French Geographic Institute from two airborne LiDAR sur-

veys carried out over La Réunion in 2008 and 2009. After georeferencing, the coherence maps derived from IW data have a 15 m pixel size, and those derived from SM data have a 5 m pixel size.

To discriminate, in the coherence images, areas covered by lava flow from other poorly coherent areas (e.g., due to air fall or to changes in the soil moisture between the two radar acquisitions) we developed a three step procedure. The first step consists of applying a median filter on the coherence image. Then, in a second step, we perform a clustering-based image thresholding approach: the Otsu algorithm (Otsu 1979). The resulting binary image is used to trace the lava flow boundary (including boundaries of kipukas) using the `bwboundaries` Matlab© function. Finally, the lava flow surface area is estimated with associated uncertainty taking into account the pixel surface and the probability that each pixel belongs to the lava flow knowing its coherence.

As the April – May 2018 eruption lasted more than one month, we were able to compute several coherence images combining, for a given acquisition geometry and mode (ascending or descending pass, IW or SM mode), a unique master image with several slave images. The master images were acquired before the beginning of the eruption and the slave images during the eruption, or just after its end. This allowed us to estimate the evolution of the lava flow surface area at different epochs (see Appendix D). Moreover, several interferograms, spanning the total duration of the eruption, were produced by combining a master image acquired before the beginning of the eruption and the slaves images acquired in the weeks following the end of the eruption. The coherence images associated with these interferograms have been stacked to produce an accurate map of the final lava flow extension and its total surface area (see Appendix D).

Generally, the lava flow field becomes coherent a few weeks to a few months after the end of the eruption (Bato et al. 2016; Chaussard 2016; Wittmann, Sigmundsson, and Lavallée 2017). The thickness of the lava flow field can be estimated from the topographical residuals in the interferograms. These residuals reflect the deviation between a reference DEM used in the interferometric processing and the actual topography (Massonnet and Feigl 1998). Since the amplitude of topographic residuals is proportional to the perpendicular baseline of the interferometric couple (Massonnet and Feigl 1998), one can obtain a relatively accurate determination of the changes in the volcano topography due to lava flow emplacement by a statistical exploitation of several interferograms covering a large range of perpendicular baseline (Bato et al. 2016). The lava thickness obtained in this way can be used not only to evaluate the volume of the lava flow field, and then, by making some assumptions on the lava porosity, the volume of lava emitted, but also to update the DEM after each eruption. Such an update is mandatory to achieve model-based flow-length projections. Unfortunately, in the case of the April 2018 eruption, we could not use the Sentinel-1 interferograms to determine the lava flow thickness since the perpendicular baseline ( $B_{\text{perp}}$ ) of the S1 interferometric couples was always very low ( $\overline{B_{\text{perp}}} = 48 \text{ m} \pm 35 \text{ m}$ ). A particular effort has been made by ESA in the Sentinel-1 system design to achieve an orbital tube of 50 m radius (rms). This guaranties high performances for ground surface displacement measurement purposes by reducing the sensibility of the interferograms to possible topographic artifacts. However, in our case, this “improvement” is a disadvantage since we are looking for topographic residuals (Ebmeier et al. 2012; Albino et al. 2015; Kubanek, Westerhaus, et al. 2015; Kubanek, Richardson, et al. 2015; Bato et al. 2016; Kubanek, Westerhaus, and Heck 2017). The characteristics of CosmoSky-Med and TerraSAR-X/TanDEM-X constellations make them better suited for this type of application. The use of future CSK and TSX/TDX acquisitions for Piton de la Fournaise will allow us to calculate the April-May 2018 lava flow thickness.

## References

- Albino, F, B Smets, N Oreye, and F Kervyn. 2015. “High-Resolution TanDEM-X DEM : An Accurate Method to Estimate Lava Flow Volumes at Nyamulagira.” *Journal of Geophysical Research : Solid Earth*, 4189–4207. doi:10.1002/2015JB011988. Received.
- Bato, M. G., J. L. Froger, A. J. L. Harris, and N. Villeneuve. 2016. “Monitoring an Effusive Eruption at Piton de La Fournaise Using

- Radar and Thermal Infrared Remote Sensing Data: Insights into the October 2010 Eruption and Its Lava Flows.” *Geological Society, London, Special Publications*. doi:10.1144/SP426.30.
- Biggs, Juliet, and Matthew E. Pritchard. 2017. “Global Volcano Monitoring: What Does It Mean When Volcanoes Deform?” *Elements* 13 (1): 17–22. doi:10.2113/gselements.13.1.17.
- Chaussard, Estelle. 2016. “Subsidence in the Paricutin Lava Field: Causes and Implications for Interpretation of Deformation Fields at Volcanoes.” *Journal of Volcanology and Geothermal Research* 320: 1–11. doi:10.1016/j.jvolgeores.2016.04.009.
- Dietterich, Hannah R., Michael P. Poland, David A. Schmidt, Katharine V. Cashman, David R. Sherrod, and Arkin Tapia Espinosa. 2012. “Tracking Lava Flow Emplacement on the East Rift Zone of Kilauea, Hawaii, with Synthetic Aperture Radar Coherence.” *Geochemistry, Geophysics, Geosystems* 13 (5): 1–17. doi:10.1029/2011GC004016.
- Ebmeier, S. K., J. Biggs, T. A. Mather, J. R. Elliott, G. Wadge, and F. Amelung. 2012. “Measuring Large Topographic Change with InSAR: Lava Thicknesses, Extrusion Rate and Subsidence Rate at Santiaguito Volcano, Guatemala.” *Earth and Planetary Science Letters* 335–336. Elsevier: 216–25. doi:10.1016/j.epsl.2012.04.027.
- Ferretti, Alessandro, Claudio Prati, and Fabio Rocca. 2001. “Permanent Scatterers in SAR Interferometry.” *IEEE Transactions on Geoscience and Remote Sensing* 39 (1): 8–20. doi:10.1109/36.898661.
- Hooper, Andrew, Howard Zebker, Paul Segall, and Bert Kampes. 2004. “A New Method for Measuring Deformation on Volcanoes and Other Natural Terrains Using InSAR Persistent Scatterers.” *Geophysical Research Letters* 31 (23): 1–5. doi:10.1029/2004GL021737.
- Kampes, Bert, and Ramon Hanssen. 2003. “Radar Interferometry with Public Domain Tools.” In *Proceedings of FRINGE 2003*.
- Kampes, Bert, and Stefania Usai. 1999. “Doris: The Delft Object-Oriented Radar Interferometric Software.” In *Proceedings ITC 2nd ORS Symposium*.
- Kubaneck, Julia, Jacob A. Richardson, Sylvain J. Charbonnier, and Laura J. Connor. 2015. “Lava Flow Mapping and Volume Calculations for the 2012–2013 Tolbachik, Kamchatka, Fissure Eruption Using Bistatic TanDEM-X InSAR.” *Bulletin of Volcanology* 77 (12): 1–13. doi:10.1007/s00445-015-0989-9.
- Kubaneck, Julia, Malte Westerhaus, and Bernhard Heck. 2017. “TanDEM-X Time Series Analysis Reveals Lava Flow Volume and Effusion Rates of the 2012–2013 Tolbachik, Kamchatka Fissure Eruption.” *Journal of Geophysical Research: Solid Earth* 122 (10): 7754–74. doi:10.1002/2017JB014309.
- Kubaneck, Julia, Malte Westerhaus, Andreas Schenk, Nurnaning Aisyah, Kirbani Sri Brotopuspito, and Bernhard Heck. 2015. “Volumetric Change Quantification of the 2010 Merapi Eruption Using TanDEM-X InSAR.” *Remote Sensing of Environment* 164. Elsevier Inc.: 16–25. doi:10.1016/j.rse.2015.02.027.
- Massonnet, Didier, Pierre Briole, and Alain Arnaud. 1995. “Deflation of Mount Etna Monitored by Spaceborne Radar Interferometry.” *Nature* 375: 375–567.
- Massonnet, Didier, and Kurt L. Feigl. 1998. “Radar Interferometry and Its Application to Changes in the Earth’s Surface.” *Reviews of Geophysics* 36 (4): 441–500. doi:10.1029/97RG03139.
- Otsu, Nobuyuki. 1979. “A Threshold Selection Method from Gray-Level Histograms.” *IEEE Transaction on Systems, Man and Cybernetics* SMC-9 (1): 62–66.
- Pinel, V., M. P. Poland, and A. Hooper. 2014. “Volcanology: Lessons Learned from Synthetic Aperture Radar Imagery.” *Journal of Volcanology and Geothermal Research* 289. Elsevier B.V.: 81–113. doi:10.1016/j.jvolgeores.2014.10.010.
- Rowland, Scott K., Andrew J.L. Harris, Martin J. Wooster, Falk Amelung, Harold Garbeil, Lionel Wilson, and Peter J. Mouginis-Mark. 2003. “Volumetric Characteristics of Lava Flows from Interferometric Radar and Multispectral Satellite Data: The 1995 Fernandina and 1998 Cerro Azul Eruptions in the Western Galápagos.” *Bulletin of Volcanology* 65 (5): 311–30. doi:10.1007/s00445-002-0262-x.
- Wittmann, Werner, Freysteinn Sigmundsson, and Yan Lavallée. 2017. “Post-Emplacement Cooling and Contraction of Lava Flows: InSAR Observations and a Thermal Model for Lava Fields at Hekla Volcano, Iceland.” *Journal of Geophysical Research B: Solid Earth*, 1–20. doi:10.1002/2016JB013444.Abstract.

## Appendix C

### Example of ASTER URP email

Given here is an example of the ASTER URP trigger for April–May 2018 eruption of Piton de la Fournaise as triggered by the University of Hawaii’s hot spot detection system, MODVOLC (Wright et al. 2002):

---

From: Thermal Hotspot Work <thermal@hotspot3.higp.soest.hawaii.edu>  
Sent: Saturday, April 28, 2018 3:25 PM  
To: daac\_alerts2@higp.hawaii.edu  
Subject: HIGP Urgent Request

---

Mike|Ramsey|Hawaii Institute of Geophysics and Planetology

|Volcano|1|21.24|1|55.71|Fournaise,\_Piton\_de\_la|Fournaise,\_Piton\_de\_la|

http://modis.higp.hawaii.edu/cgi-bin/mergeimage?  
mapttype=relief&jyear=2018&jday=116&jperiod=4.0&lonmin=55.658&lonmax=55.758&latmin=-  
21.294&latmax=-21.194&xsize=600&ysize=600

|Indian\_Ocean\_(western)|Middle\_East\_and\_Indian\_Ocean|Day|fullmode|Yes|Normal|Yes|Normal  
|Normal|Normal|Normal|Normal|Normal|Normal|Normal|Normal|UTM

|Cubic Convolution|Immediately on receipt of data| ||Volcano monitoring|HIGP Urgent Request

|mramsey@pitt.edu

---

The automatic response to this notification from the URP system was as follows :

---

**From:** aesics@usgs.gov <aesics@usgs.gov>  
**Sent:** Saturday, April 28, 2018 3:31 PM  
**Subject:** AESICS - New Request: Fournaise,\_Piton\_de\_la

---

A new request has been received by AESICS and is pending approval. The full request details and/or update the request, [click here](#).

### Overview

**DAAC ID:** 26392

**STAR ID:** None

**Event Name:** Fournaise,\_Piton\_de\_la

**Application:** Volcano

**Justification:** Volcano monitoring

## **Location**

**Event Country:** Indian\_Ocean\_(western)

**Event Location:** Middle\_East\_and\_Indian\_Ocean

**Coordinates:** ([-21.24, 55.71](#))

**Reference URL:** [Link](#)

## **Acquisition and Processing**

**Sensor Mode:** full mode

**Local Time:** Night

**Off-NADIR Ok:** yes

**Off-NADIR Amount:** Normal

**Processing Urgency:** Expedited

## **Gain Settings**

**VNIR1:** normal

**VNIR2:** normal

**VNIR3:** normal

**SWIR4:** normal

**SWIR5:** normal

**SWIR6:** normal

**SWIR7:** normal

**SWIR8:** normal

**SWIR9:** normal

**LAVA FLOW FIELD REPORTING FORM**  
 (file name save format: yyyyymmdd-Volcano name-ANR-LAVA-REPORT-##)

Target	Piton de la Fournaise
Eruption Start Date and Time (local)	2018-04-27-T-23:50 (local time)
Report Date and Time (UTC)	2018-07-11-T-12:00 (GMT)
Up-dated by	HARRIS Andrew

**Field 1: TIME-AVERAGED DISCHARGE RATE**

Sensor	MODIS
Processing System	MIROVA
Last update	2018-05-24T06:10:00
Up-dated by	COPPOLA Diego

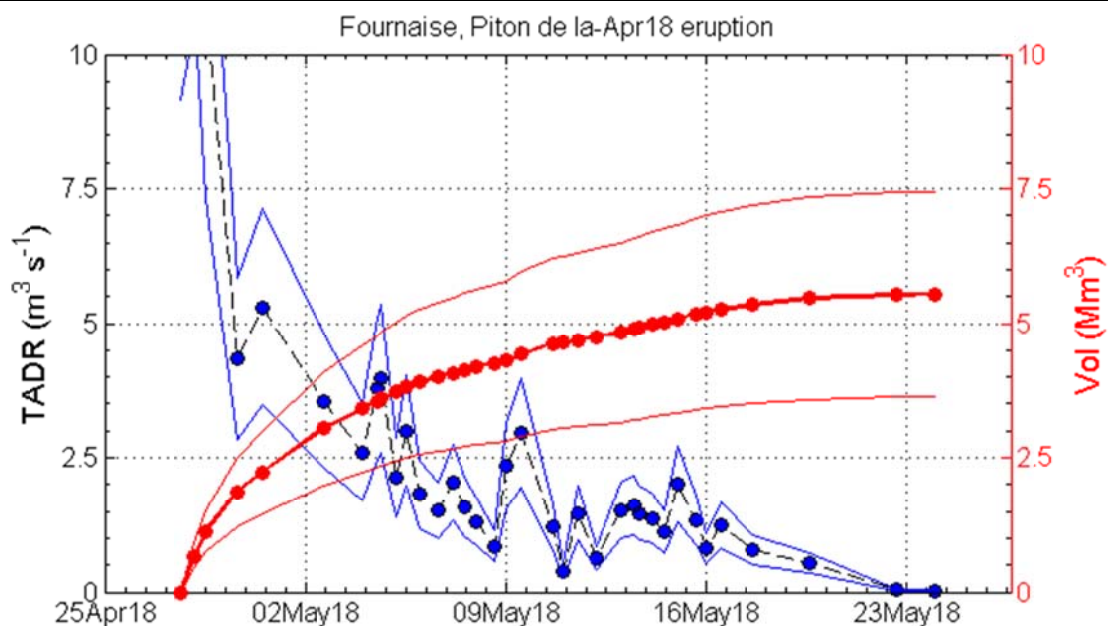
Image Date	Image Time	TADR-min	TADR-max
15-05-2018	06:15:00	1.32	2.71
15-05-2018	21:30:00	0.88	1.81
15-05-2018	21:30:00	0.88	1.81
16-05-2018	06:55:00	0.53	1.09
16-05-2018	19:05:00	0.82	1.69
16-05-2018	19:05:00	0.82	1.69
17-05-2018	21:20:00	0.51	1.05
19-05-2018	21:05:00	0.35	0.73
22-05-2018	21:35:00	0.02	0.04
24-05-2018	06:10:00	0.02	0.03

**Comments:**

The MODIS image acquired today at 06:10 UTC, indicates very low levels of thermal activity over the lava field (~5 MW) corresponding to a very low TADR (0.015 to 0.03 m<sup>3</sup>/s). However, this low thermal flux could be also related to the cooling of the lava field emplaced in the previous days; meaning there is the possibility that there is no flow so the TADR is "false"; it being derived from a cooling anomaly.

**Time Series:**

Start date	Current date	No. data points	Duration
2018-04-27T21:45	2018-05-24T06:10	35	27



## Field 2: FLOW SIMULATION

Last update		<2018-06-21-T-15-00>	
Up-dated by		CHEVREL Oryaëlle	
Flow path model		DOWNFLOW	
<b>DEM file</b>	DEM resolution	Noise	No. iterations
5m_updated.asc	5 m	±0.001 – 1m	1000
Vent location	Source: airborne GPS	Source: field GPS	Source: ASTER
365377; 7648853	N	Surveillance camera	N
40 K (Google Earth)	2018-04-28	04:33 (local time)	OVPF
Flow length model		PyFLOWGO	
Initialization file		Same as 2010 eruption	
Run Date	TADR used	Channel dimension	Run out
2018-06-22	20m <sup>3</sup> /s	3 × 1.5	1100 m
Flow projection map:			
Vent position	Current run date	TADR used	Eruption temperature
365377; 7648853<UTM>	2018-06-22	20 m <sup>3</sup> /s	1114°C
<p>Solution for a constant effusion rate of approx 20.3 m<sup>3</sup>/s and a source channel width of 3.00 m and 1.500 deep</p> <p>Slope profile</p>		<p>Legend</p> <ul style="list-style-type: none"> <li>Main path (D=0.001, N=1, Df = 1; N = 1000)</li> <li>run out distance 21m<sup>3</sup>/s</li> <li>Runout distance for given effusion rate in m<sup>3</sup>/s</li> <li>Steepest slope path</li> <li>vent_location_surveillance_camera</li> </ul>	

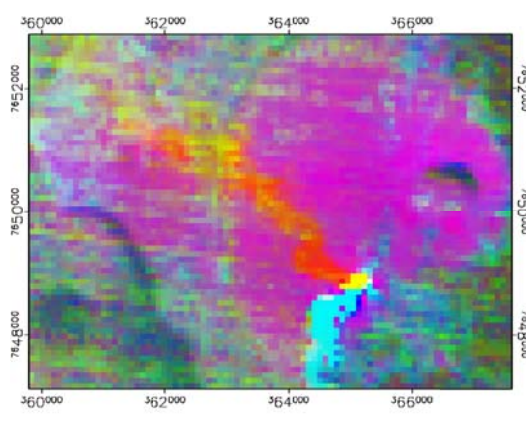
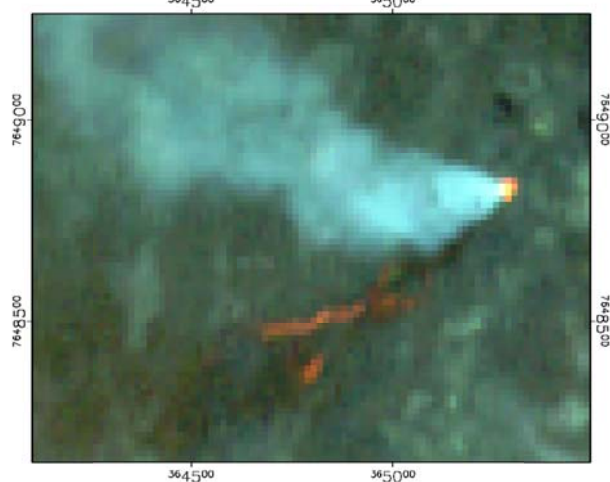
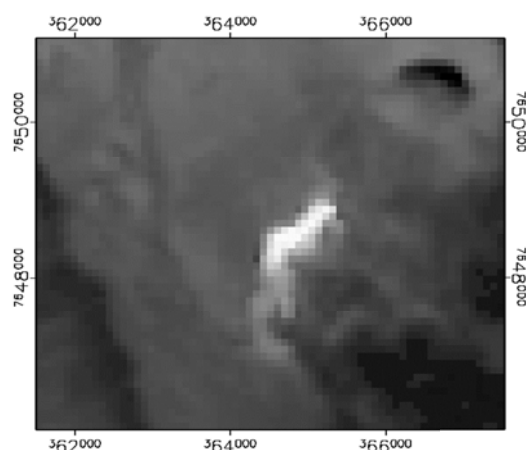
### Comments:

Initial vent position is based on the middle of the main fissure as apparent in the web-cam data and projected onto GOOGLE EARTH. This will need checking and updating : **TREAT WITH CAUTION**  
**The DOWNFLOW path** has been modified by hand to remove the lava ponding effect (green in graph) and then the slope was smoothed every 10 m (blue in graph).



### Field 3: ASTER

Last update		<2018-05-24T06:10:00>	
Up-dated by		RAMSEY Michael	
Image date	Image time (UT)	TADR (m <sup>3</sup> /s)	SO <sub>2</sub> flux (kg/s)
04-05-2018	06:34:00	<i>not calculated</i>	<i>not calculated</i>
Image date	Image time (UT)	Anomaly Length (m)	Anomaly Area (m <sup>2</sup> )
02-05-2018	06:15:00	1367	281,411
04-05-2018	06:34:00	2446	553,918
09-05-2018	19:03:00	4107	1,098,212
25-05-2018	19:03:00	4301	973,751
ASTER hot spot map:			
Image date	Image time (UT)	VNIR bands used	TIR bands used
04-05-2018	06:34:00	<b3; b2; b1>	b13 / b13; b11; b10



#### Comments:

4 May 2018 ASTER VNIR (left) and TIR (right) data shown. First ASTER full mode (VNIR + TIR) acquisition following URP trigger. Vent location verified in the VNIR data along with the presence of open channels. TIR anomaly length + area includes all pixels above background, not just the saturated pixels corresponding to open channel location. TIR decorrelation stretch color composite confirms SO<sub>2</sub> in plume (yellow/orange). Note: TADR and SO<sub>2</sub> flux values were not calculated.

## Field 4: INSAR

Last update	2018-07-06-T-15-00
Up-dated by	Alexis HRYSIEWICZ
Processing System	Doris 5.0 and Matlab

	Satellite	Mode (track)	Date	time
Master	S1B	SM (151)	2018-04-16	01:46:38.148088
Slave	S1B	SM (151)	2018-04-28	01:46:38.734417
Dimensions:	Length =	1.8 km	Area =	$0.5 \times 10^6 \text{ m}^2 \pm 0.1 \times 10^6$
Master	S1A	IW (144)	2018-01-03	14:53:10.372910
Slave	S1A	IW (144)	2018-05-03	14:53:11.013571
Dimensions:	Length =	2.5 km	Area =	$1 \times 10^6 \text{ m}^2 \pm 0.3 \times 10^6$
Master	S1B	SM (151)	2018-04-16	01:46:38.148088
Slave	S1B	SM (151)	2018-05-10	01:46:39.238256
Dimensions:	Length >	3.5 km	Area =	$1.2 \times 10^6 \text{ m}^2 \pm 0.2 \times 10^6$
Master	S1A	IW (151)	2018-05-04	01:47:32.171178
Slave	S1A	IW (151)	2018-05-16	01:47:32.875454
Dimensions:	Length =	4.1 km	Area =	$1.3 \times 10^6 \text{ m}^2 \pm 0.3 \times 10^6$

### InSAR coherence and flow area maps:

	Satellite	Mode	Date	time
Master	S1B	SM (144)	2018-04-27	14:52:39.557416
Slave	S1B	SM (144)	2018-06-26	14:52:43.052570

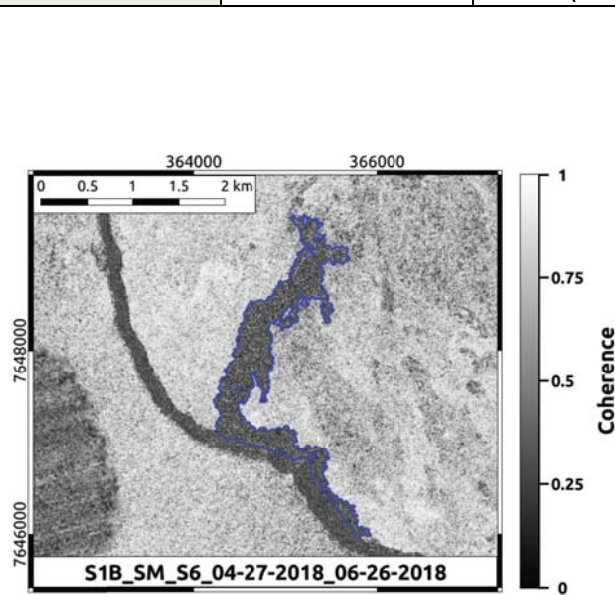


Fig 1: Coherence image between April 27, 2018 and June 26, 2018. The final lava flow contour extracted from InSAR is given with the blue line.

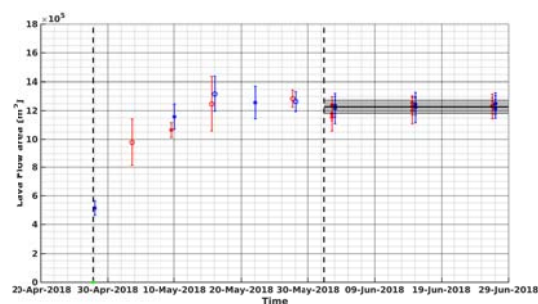


Fig 2: Evolution of the lava flow area from InSAR. The stars correspond to the Sentinel 1 SM data, the circles are for the Sentinel 1 IW data. The blue color is used to denote the Descending acquisitions, and the red is for Ascending images. The black line is the final computed area obtained from several coherence images covering the entire eruption duration. The error bars are set as two times the standard deviation. The gray zone marks the uncertainty on the final area.

### Comments: